nature photonics

Article

https://doi.org/10.1038/s41566-024-01549-1

Integrated non-reciprocal magneto-optics with ultra-high endurance for photonic in-memory computing

Received: 18 January 2024

Accepted: 14 September 2024

Published online: 23 October 2024

Check for updates

Paolo Pintus[1,2] ✉, Mario Dumont[1], Vivswan Shah[3], Toshiya Murai[4], Yuya Shoji[5], Duanni Huang[1], Galan Moody[1], John E. Bowers[1] & Nathan Youngblood[3] ✉

Processing information in the optical domain promises advantages in both speed and energy efficiency over existing digital hardware for a variety of emerging applications in artificial intelligence and machine learning. A typical approach to photonic processing is to multiply a rapidly changing optical input vector with a matrix of fixed optical weights. However, encoding these weights on-chip using an array of photonic memory cells is currently limited by a wide range of material- and device-level issues, such as the programming speed, extinction ratio and endurance, among others. Here we propose a new approach to encoding optical weights for in-memory photonic computing using magneto-optic memory cells comprising heterogeneously integrated cerium-substituted yttrium iron garnet (Ce:YIG) on silicon micro-ring resonators. We show that leveraging the non-reciprocal phase shift in such magneto-optic materials offers several key advantages over existing architectures, providing a fast (1 ns), efficient (143 fJ per bit) and robust (2.4 billion programming cycles) platform for on-chip optical processing.

The growing divide between the demand for computing resources and the performance of digital hardware necessitates the development of post-complementary metal–oxide–semiconductor (CMOS) architectures that can achieve ultra-high computational throughput at ultra-low energies. An extreme example of this comes from the field of deep learning, where the computation required to train state-of-the-art deep neural networks grew by over 300,000× between 2015 and 2020, doubling every 3.4 months[1,2], whereas the efficiency of graphics processing units (GPUs) grew[3–5] by only 300-fold. Many distinct photonic architectures have been proposed and demonstrated to attempt to address this major bottleneck facing the field of AI and computing[6], namely, matrix-vector multiplication (MVM). The vast majority of these approaches can be classified as weight-stationary photonic processors[7], where a matrix of programmable optical weights—typically encoded in a 2D array of non-volatile memory elements or optical modulators[8–15]—is used to perform a linear transformation on a vector of optical inputs. This design approach has the benefit of performing computation in the memory array itself, not unlike analogue computing in the electrical domain using crossbar arrays of resistive random access memory (RRAM), which can substantially reduce data movement and latency while improving energy efficiency[16].

However, a crucial (yet seldom mentioned) limitation of these weight-stationary approaches is the time and energy required to update the fixed weights of the matrix to implement useful computing

[1]Department of Electrical and Computer Engineering, Univ. of California, Santa Barbara, CA, USA. [2]Department of Physics, University of Cagliari, Cagliari, Italy. [3]Department of Electrical and Computer Engineering, Univ. of Pittsburgh, Pittsburgh, PA, USA. [4]Platform Photonics Research Center, National Institute of Advanced Industrial Science and Technology (AIST), Ibaraki, Japan. [5]Laboratory for Future Interdisciplinary Research of Science and Technology, Department of Electrical and Electronic Engineering, Tokyo Institute of Technology, Tokyo, Japan. ✉e-mail: paolo.pintus@unica.it; nathan.youngblood@pitt.edu

https://doi.org/10.1038/s41566-024-01549-1

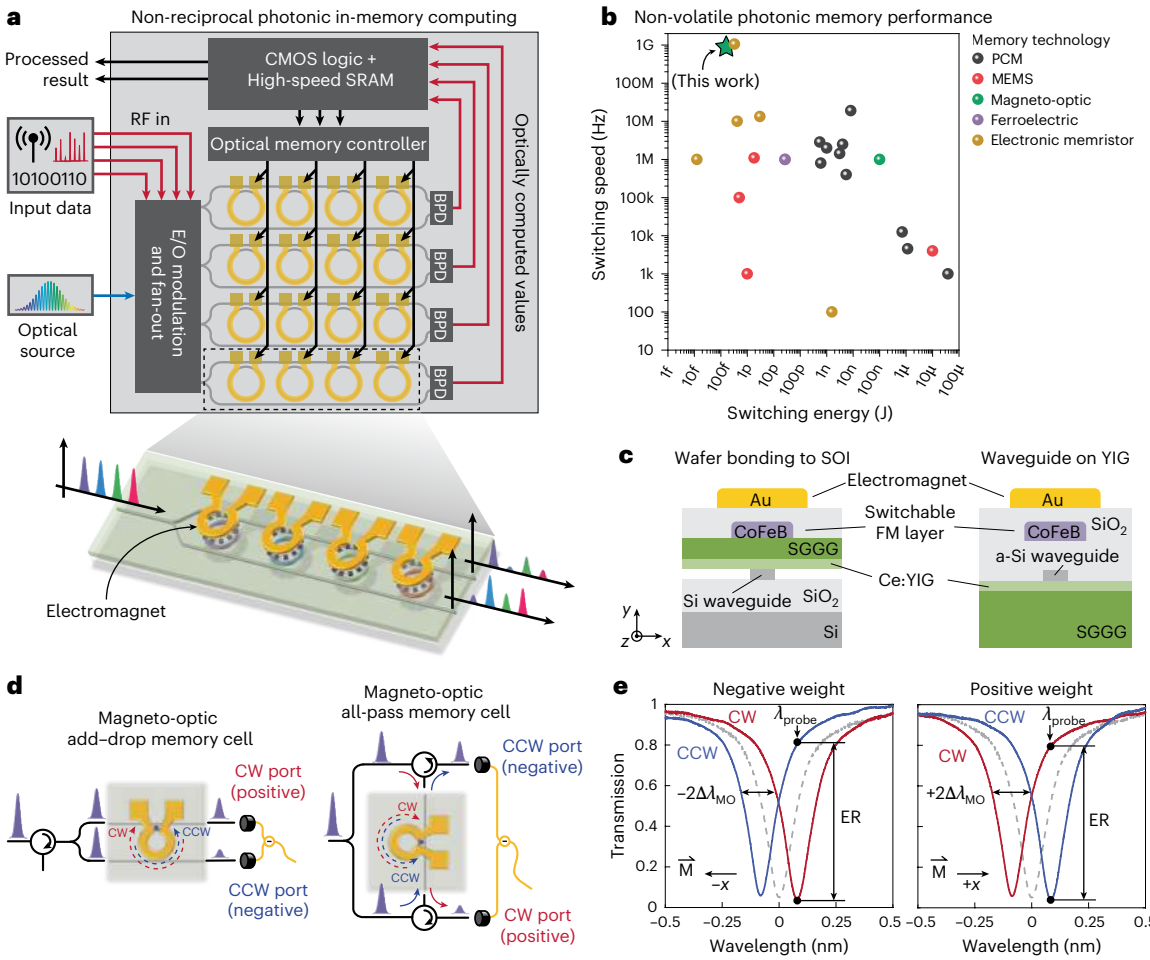

Fig. 1 | Non-reciprocal photonic in-memory computing. a, Our vision for a non-reciprocal photonic computing platform that leverages high-speed magneto-optic memory arrays to enable fast weight updates. In this platform, radio frequency (RF), analog or digital electronic signals are converted to the optical domain through electro-optic (E/O) modulators. A single row from our proposed architecture, which leverages non-reciprocal memory cells to compute a dot-product optically, is illustrated below. Balanced photodetectors (BPDs) convert the differential optical signal back to the electrical domain which then can be further processed using CMOS logic coupled to high-speed, static random-access memory (SRAM). **b**, Speed versus energy comparison of state-of-the-art non-volatile photonic memory technologies that have been demonstrated on-chip. **c**, Cross-section of non-reciprocal magneto-optic memory. Either wafer bonding and chemical mechanical polishing (left) or growth and patterning of amorphous silicon on Ce:YIG substrates (right) can be used to heterogeneously integrate Ce:YIG with silicon waveguides. In both cases, high-quality Ce:YIG is guaranteed by growing the garnet on a native substrate of substituted gadolinium gallium garnet (SGGG). SOI, silicon-on-insulator. **d**, Illustration of two implementations used to demonstrate magneto-optic memory cells where both counter-propagating modes are excited in the MRR. Optical circulators are used to prevent back reflection to the optical source during measurements. **e**, Positive and negative weights are encoded by switching the magnetization direction and amplitude, which results in opposite resonance shifts for the CW and CCW counter-propagating modes.

algorithms. Unlike electronic crossbar arrays, which aim to fully map the entire neural network into analogue weight banks to minimize reprogramming of the array, optical weight banks have much lower storage density (for example, ~0.01 bits μm^{-2}; ref. 17) and can only store a tiny fraction of the necessary parameters on-chip (for example, a 16 × 16 phase-change memory array[18] or 64 × 64 Mach–Zehnder interferometer array[8]). Thus, to accommodate the large number of parameters required by real-world applications, the photonic weight bank must be reprogrammed many times for each matrix operation that exceeds the dimensions of the weight bank. This requires photonic memory cells that can be deterministically programmed quickly, efficiently and with high endurance, or they will dramatically reduce throughput and energy efficiency of the entire system[7,19,20].

To address these challenges, we propose a resonance-based photonic architecture (inspired by the broadcast and weight design[9]) that leverages the non-reciprocal phase shift in magneto-optical materials to implement photonic in-memory computing. In this architecture (Fig. 1a) we excite both the clockwise (CW) and counterclockwise (CCW) modes of a micro-ring resonator (MRR) with a magneto-optic cladding layer (cerium-substituted yttrium iron garnet or Ce:YIG). The interaction between the optical mode and Ce:YIG causes a non-reciprocal phase shift for the two counter-propagating modes, which is visible as a split resonance shift with opposite signs, dependent on the direction and strength of an applied magnetic field. This approach has several benefits. First, we can efficiently achieve programming speeds of ~1 GHz, non-volatility, and multi-level encoding, as demonstrated in this work (see Fig. 1b and Table 1 for a comparision with the state of the art). Second, the cycling endurance of magnetic-based memory is known to be orders of magnitude greater than competing technologies[21], an outstanding challenge for many non-volatile optical memories[22]. Finally, unlike add–drop MRR weights that are based on reciprocal optical effects[9] (for example, thermo-optic or plasma-dispersion effects), the differential signal is measured from the through-port transmission for both the CW and CCW modes, improving the symmetry and extinction ratio for both positive and negative weighting.

Table 1 | Comparison of electrically programmable, non-volatile memory technologies that have been experimentally demonstrated on an integrated photonic platform

Memory technology	Switching speed	Switching energy (J bit^{-1})	Bit precision	Footprint (μm^2)	ER (dB)	IL (dB)	Switching cycles	Ref.
Trapped charge	0.6 s	Set: 17.2 pJ Reset: 11.4 pJ	4-bits	314	13	2	>30	38
MEMS	–[a]	–[a]	1-bit	8,400	37	0.13	100	39
Ferroelectric (HZO)	>1 s	–[a]	1-bit	~2,000,000	40	2.75	–	40
Ferroelectric (BTO)	1 μs[b]	4.6 pJ	3-bits	>20,000	12	>0.07	300	41
PCM	408 ns 220 μs	Am: 5.55 nJ Cry: 753 nJ	3.5-bits	4.73	~3	~1	1,500	42
PCM	50 ns 200 ns	Am: 8.8 nJ Cry: 6.9 nJ	4-bits	25	4.13	1.78	100	35
Memristor	1 μs	12.5 fJ	1-bit	0.12	9.2	25	1,000	43
Memristor	100 ns	Set: 1.3 pJ Reset: 400 fJ	1-bit	314	~12	~5	800	33
Memristor	0.3 ns 0.9 ns	Set: 150 fJ Reset: 360 fJ	1.5-bit	314	~14	~2	1,000	32
Magneto-optic	1 ns	143 fJ	3.5-bits	4,900	16.2	1.8	2.4 billion	This work

ER, extinction ratio; IL, insertion loss; MEMS, micro-electromechanical systems; PCM, phase-change material. [a]Switching speed and energy not reported. [b]Ferroelectric BTO requires a 0.7 s initialization procedure prior to writing the final state.

Device design

Integration of the Ce:YIG layer with the photonic circuit can be achieved either through wafer bonding and polishing[23], or by deposition and patterning of an amorphous silicon layer[24] (Fig. 1c). Programming the state of the memory cell requires a radial in-plane magnetic field that is supplied by an integrated gold electromagnet. To maintain a non-volatile state without dissipating power, a ferromagnetic thin-film (CoFeB) patterned into an array of bar magnets can be integrated with the electromagnet on-chip[24,25]. A magneto-optic memory cell can be implemented using either the add–drop MRR or all-pass MRR configurations (Fig. 1d). Figure 1e shows example spectra from a non-reciprocal memory cell under a negative (left) and positive (right) radial-applied magnetic field. In the case of positive magnetization ($M_x > 0$), the forward propagating CCW mode (that is, same propagation direction as current flow in the electromagnet) red-shifts while the CW mode blue shifts. If the optical probe is red detuned from resonance when $M_x = 0$, the resulting differential transmission encodes a negative weight. The opposite is true for negative magnetization ($M_x < 0$). For a critically coupled MRR, this approach can achieve high transmission contrast, limited by the extinction ratio of the CW and CCW modes.

The functionality of our non-reciprocal memory cell can be extended beyond the single dot-product shown in Fig. 1a to MVM operations. In Fig. 2 we compare two broadcast and weight architecture designs featuring non-reciprocal (Fig. 2a) and reciprocal (Fig. 2b) MRR-based weights. Here, the matrix operation $W\mathbf{x} = \mathbf{b}$ is achieved through fan-out of the optical input vector to each row of W. This input vector is then multiplied by the wavelength-dependent transmission of each resonator in the row before being summed through incoherently combining the transmitted power at each row's pair of output waveguides as originally proposed by Tait and co-workers[9]. An important distinction between the two approaches can be visualized in the transmission spectra of the bus waveguides. Although the differential photocurrent compares the CW and CCW through ports in Fig. 2a, the differential transmission of the through and drop ports is used to compute $\mathbf{b}$ in Fig. 2b. This is an important distinction because the drop port of the reciprocal MRR weight reaches its maximum extinction ratio at a phase shift of π when the optical probe is centred at resonance. Thus, to achieve high optical contrast between the through and drop ports (that is, to improve the bit precision of the weight), a much larger phase shift is required in the case of a reciprocal MRR compared with a non-reciprocal MRR. Although this may not be a limiting factor for a single memory cell, reducing the phase shift required to achieve the full range of positive and negative weight values in the array reduces the optical cross-talk between neighbouring resonances[26] and alleviates the challenge of achieving strong optical modulation on-chip.

This distinction is highlighted in Fig. 2c–f where we simulate the differential transmission of both reciprocal and non-reciprocal optical memory with the same quality factor ($Q = 10{,}000$). In Fig. 2c we see that the differential transmission for both positive and negative values is an anti-symmetric function centred at $\phi = 0$. This function is shown in Fig. 2d for three different optical probe wavelengths: 0.5×, 1.0× and 1.5× the full-width half maximum (FWHM) linewidths red detuned from resonance when $\phi = 0$. As the detuning of the probe increases, the maximum and minimum weight values increase in magnitude, while the linearity of the weighting function near $\phi = 0$ decreases. The differential transmission for the case of a reciprocal memory cell is shown in Fig. 2e. The reciprocal weighting function is symmetric and centred at $\phi = 0$, requiring a resonance shift of ~0.5 × FWHM to reach negative values when the probe is centred at resonance (Fig. 2f). Thus, to achieve an equal range of positive and negative weights (that is, minimal power penalty[26]), a phase shift of $\Delta\phi = 0.17\pi$ is required for an ideal reciprocal MRR with the same quality factor of $Q = 10{,}000$.

Modelling and experimental results

The current in the integrated electromagnet used to control the resonance of the MRR gives rise to a magnetic field and a Joule heating effect. A comprehensive model of the magneto-optic and thermo-optic effect is provided in Supplementary Section 1. The modelling results of Fig. 2 were experimentally verified for a MRR with a Ce:YIG layer ($Q \approx 10{,}000$) and an integrated electromagnet. For this demonstration, the ring radius is 35 μm and the waveguide cross-section is a 600 nm × 220 nm silicon ridge with a 400-nm-thick top-cladding of Ce:YIG. A 10-nm-thin silicon oxide layer separates the silicon from the Ce:YIG layer (see Supplementary Section 1.4). Figure 3a shows the optical transmission spectra for the fundamental transverse magnetic CW and CCW propagating modes as a function of applied current. The resonance position of the spectra shows both a linear and quadratic dependence on the applied current corresponding to the magneto- and thermo-optic effects, respectively. In Fig. 3b,c we separate the

https://doi.org/10.1038/s41566-024-01549-1

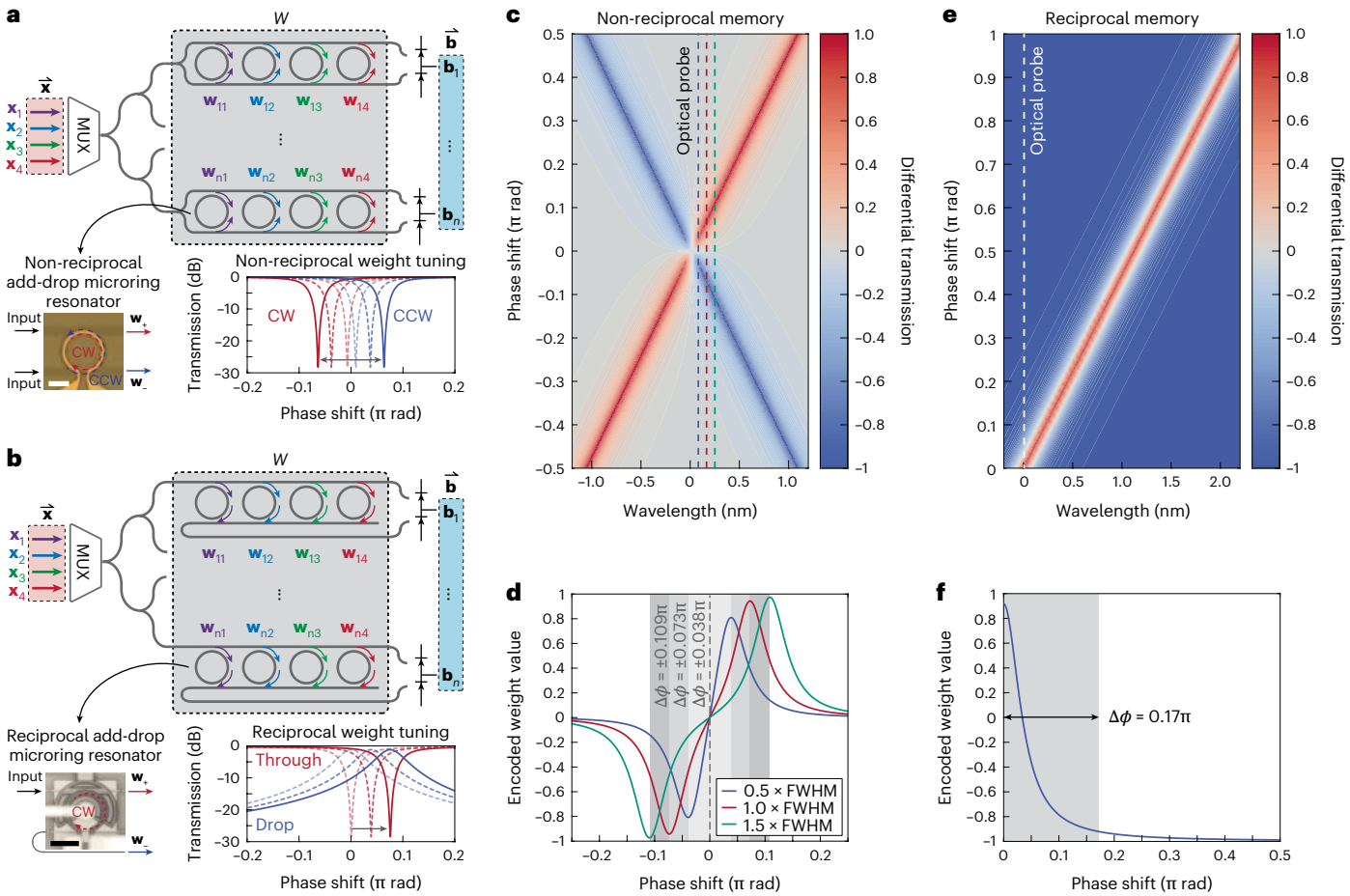

Fig. 2 | Reciprocity in photonic computing. a, Non-reciprocal photonic computing platform leveraging an integrated magneto-optic memory array. Matrix-vector multiplication is achieved by taking the differential transmission between the CW and CCW propagating modes. Scale bar, 30 µm. **b**, Reciprocal 'Broadcast and weight' architecture, which uses the difference between the through and drop ports of an add–drop MRR (scale bar, 15 µm) to encode the values of matrix *W*. In both approaches, a wavelength multiplexer (MUX) is used to combine the input optical signals into a single waveguide. **c**, Simulated map of differential through-port transmission for a non-reciprocal memory cell with $Q = 10{,}000$. **d**, Encoded weight value of non-reciprocal memory cell for an optical probe spaced 0.5, 1.0 and 1.5 FWHM away from resonance (dashed lines in **d**). Notably, the encoded value is an anti-symmetric function centred at zero phase shift. **e**, Simulated map of the difference between the through and drop ports of a reciprocal memory cell with $Q = 10{,}000$. **f**, Encoded weight value of reciprocal memory cell when the optical probe is held at resonance (white dashed line in **e**). A larger phase shift is needed to achieve symmetric weighting compared to the non-reciprocal case.

resonance shifts of the CW and CCW modes into their non-reciprocal (magneto-optic) and reciprocal (thermo-optic) components. Although the thermo-optic effect red-shifts both the CW and CCW spectra, the magneto-optic effect induces shifts in opposite directions for the two modes. For a set current, the thermo-optic shift is estimated as the average shift of the two spectra compared with the no-current scenario. The magnitude of the magneto-optic shift is half of the measured resonance split between the CW and CCW modes. In Fig. 3b,c we overlay the mathematical model with the measurement results, showing an excellent agreement between theory and experiments. Figure 3d plots the FWHM linewidth of the resonator for the CW and CCW modes, showing a similar quality factor for both modes. By varying the applied current in the electromagnet, we observe slight changes in the extinction ratio in Fig. 3a and linewidth in Fig. 3d. These variations are caused by the non-reciprocal loss in the Ce:YIG, where the optical loss changes depending on the direction of light propagation and the transverse magnetic field[27–29]. Please refer to Supplementary Section 1 for more details.

In Fig. 3e we plot the differential optical transmission of the CW and CCW modes for three different optical probe wavelength positions: 0.5×, 1.0× and 1.5× the FWHM linewidths red detuned from resonance when $\phi = 0$ (that is, no magnetic field). As expected, there is good overlap between the experimental results and the simulated weighting functions for the scenario of an ideal resonator with a similar quality factor (Fig. 2d). Again, we see that increasing the red detuning of the optical probe increases the dynamic range of the weight function due to reduced insertion loss while also decreasing the linearity between the maximum and minimum weight values. At larger current values, we observe a deviation from the expected weight value. We attribute this to the fact that, for large detuning, the two modes have different FWHM, as shown in Fig. 3d, resulting in a distinct weighting for the two directions.

Having characterized the steady-state response of our non-reciprocal optical memory, we next demonstrate high-speed weight updates through characterization of the memory cell's dynamic response. For high-speed characterization beyond ~1 MHz, the magneto-optic response dominates while the dynamic thermo-optic response becomes negligible. This can be seen in Fig. 4a, in which the dynamic optical transmission of a CW probe for two current pulses can be observed at different time scales (1 ms versus 10 ns pulse width). In the case of a slow 1 ms current pulse, the optical transmission includes both a blue shift (increase in transmission) from the fast

https://doi.org/10.1038/s41566-024-01549-1

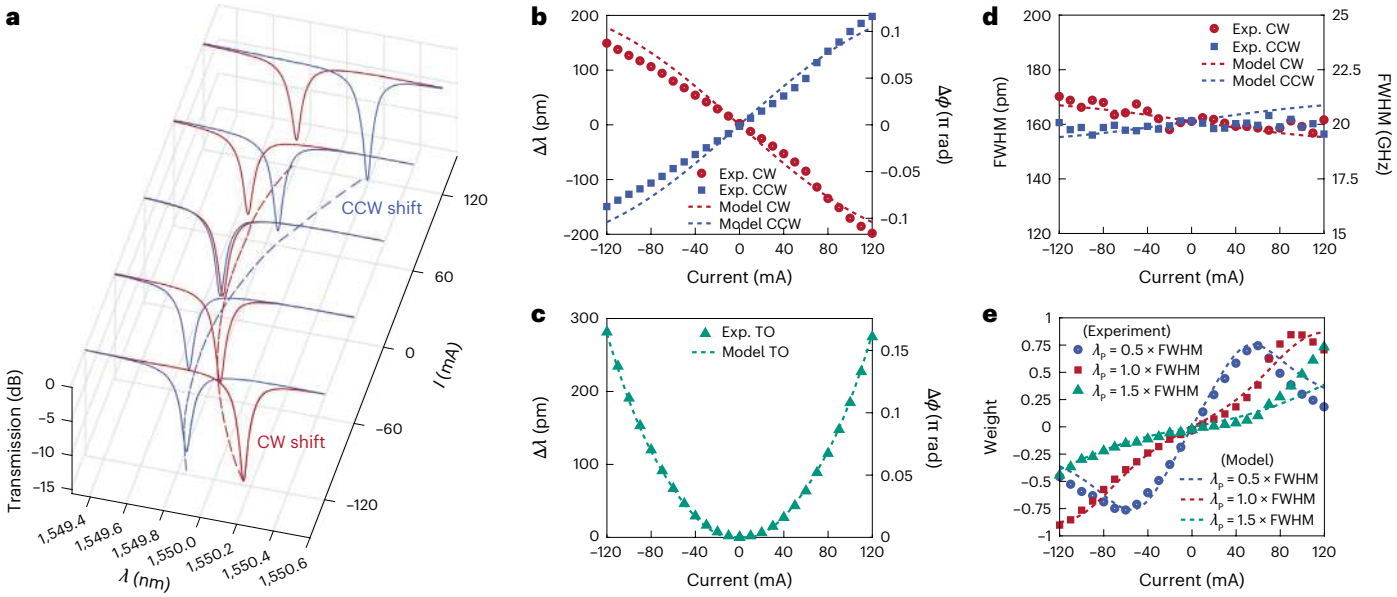

Fig. 3 | Experimental characterization of non-reciprocal optical memory. **a**, Spectral response of a non-reciprocal magneto-optic memory cell for different fixed currents ($Q \approx 10{,}000$). Both linear and quadratic resonance shifts are observed due to the magneto-optic and thermo-optic effects, respectively. **b**, Magneto-optic spectral shift for the CW and CCW modes. Dashed lines correspond to our analytical model of the expected magneto-optic phase shift excluding thermal effects. **c**, Thermo-optic phase shift (extracted from **a**) resulting from heating the electromagnet while a constant current is applied. **d**, Extracted resonance linewidth as a function of applied current for the CW and CCW modes. Slight changes in the non-reciprocal loss for different propagation directions change the quality factor of the MRR. **e**, Encoded weight for a probe wavelength (λ_p) red-detuned 0.5×, 1.0× and 1.5× FWHM away from the central resonance when no magnetic field is applied. Experimental weight values are in good agreement with the modelled results in Fig. 2d.

magneto-optic response and a red shift (decrease in transmission) from the slow thermo-optic response. For a fast current pulse and red-detuned probe, the slow decay from the thermal response of the ring disappears (rise time ≈ 50 µs and fall time = 92 µs), and we only observe the fast magneto-optic response with a rise and fall time of less than 1 ns, and a ferromagnetic resonance of 0.55 GHz. As the estimated time response of the integrated electromagnet circuit is 6 ps, the ringing observed in the optical response is attributed to magneto-optic response of the Ce:YIG, resulting in a rise/fall time of 0.95 ns (see Supplementary Section 3 for more details).

Due to the high-speed magneto-optic response and the soft in-plane magnetic axis of the Ce:YIG, the memory cell can be programmed with low energy. Figure 4b,c shows open eye diagrams measured for both the CW and CCW optical probe for 500 Mbps and 1 Gbps modulation speeds (see Supplementary Section 2 and Supplementary Fig. 5 for details on the measurement set-up). From Fig. 4b we can see that for a weight update rate of 500 Mbps (that is, 2 ns pulse width), we can achieve an open eye diagram with an extinction ratio as high as 8.3 dB for a programming energy as low as 2.28 pJ. Reducing the pulse width to 1 ns and the amplitude by half reduces the programming energy to a mere 298 fJ (Fig. 4c). This corresponds to a ~8× improvement in energy efficiency because $E_b = I^2R \times \Delta t + LI^2/2$, where E_b is the energy per bit, I is the programming current, R is the resistance of the electromagnet (~1.43 Ω), L is the inductance (0.3 nH) and Δt is the duration of the programming pulse. It is also worth noting that for our non-reciprocal memory cell, we achieve substantial modulation of the optical signal with a peak voltage as low as ±21.5 mV for ±13.8 mA current pulses, representing an extremely low programming voltage that is compatible with the most advanced CMOS nodes.

In Fig. 4d,e we demonstrate multi-level optical weighting using a four-level (2-bit) pulse amplitude modulation (PAM4) programming signal with maximum current amplitude of ±13.8 mA, corresponding to a record low programming energy of 143 fJ per bit. In these experiments we capture the transmission of the CW and CCW modes simultaneously using the experimental set-up described in Supplementary Fig. 6. The differential transmitted power between the CW and CCW modes is shown in Fig. 4e, in which we clearly observe four distinct transmission levels, allowing us to achieve to two positive and two negative optical weights given our 2-bit electrical input. Using the high-speed magneto-optic effect, we can achieve optical weight updates as fast as 1 ns, as shown in Fig. 4f,g. In our case, the maximum programming speed is limited by the ferromagnetic resonance of the Ce:YIG. Although in this device the maximum time response is 1 GHz, a much faster programming speed can be reached using other magneto-optic material systems that can support modulation rates of tens of gigahertz[30,31].

In a final demonstration, we show the non-volatile response of our non-reciprocal memory cell when integrated with a switchable ferromagnetic layer. In this experiment, patterned CoFeB magnetic stripes are integrated in the cladding above the MRR to provide a programmable, non-volatile magnetic field. The shape anisotropy and orientation of the micrometre-sized CoFeB bar magnets provides the static radial magnetic field needed to induce a non-reciprocal optical phase shift in the memory cell[24]. In this demonstration, the silicon MRR has a cross-section of a 1,000 nm × 220 nm with a radius of 50 µm. The measurement set-up and cross-section of our device are shown in Fig. 5a. To program the state of the memory cell, current is applied to the integrated electromagnet that encodes the magnetic field strength in the CoFeB magnetic domains. After the current is removed, the laser is swept to obtain the non-volatile MRR spectral shift of the CW mode (Fig. 5c–e). For an optical probe positioned at the resonance dip of the MRR (dashed lines in Fig. 5c,d), we observe the hysteretic behaviour in the optical transmission shown in Fig. 5b. When the programming current is increased from negative to positive values, we observe an increase in optical transmission for currents greater than 0 mA (red points in Fig. 5b). The transmission eventually saturates above 200 mA and remains constant due to saturation of the CoFeB magnetic layer (see the illustration in Fig. 5a). As we change the direction of the applied current from positive to negative values, the transmission remains constant until negative current values, highlighting the non-volatile

https://doi.org/10.1038/s41566-024-01549-1

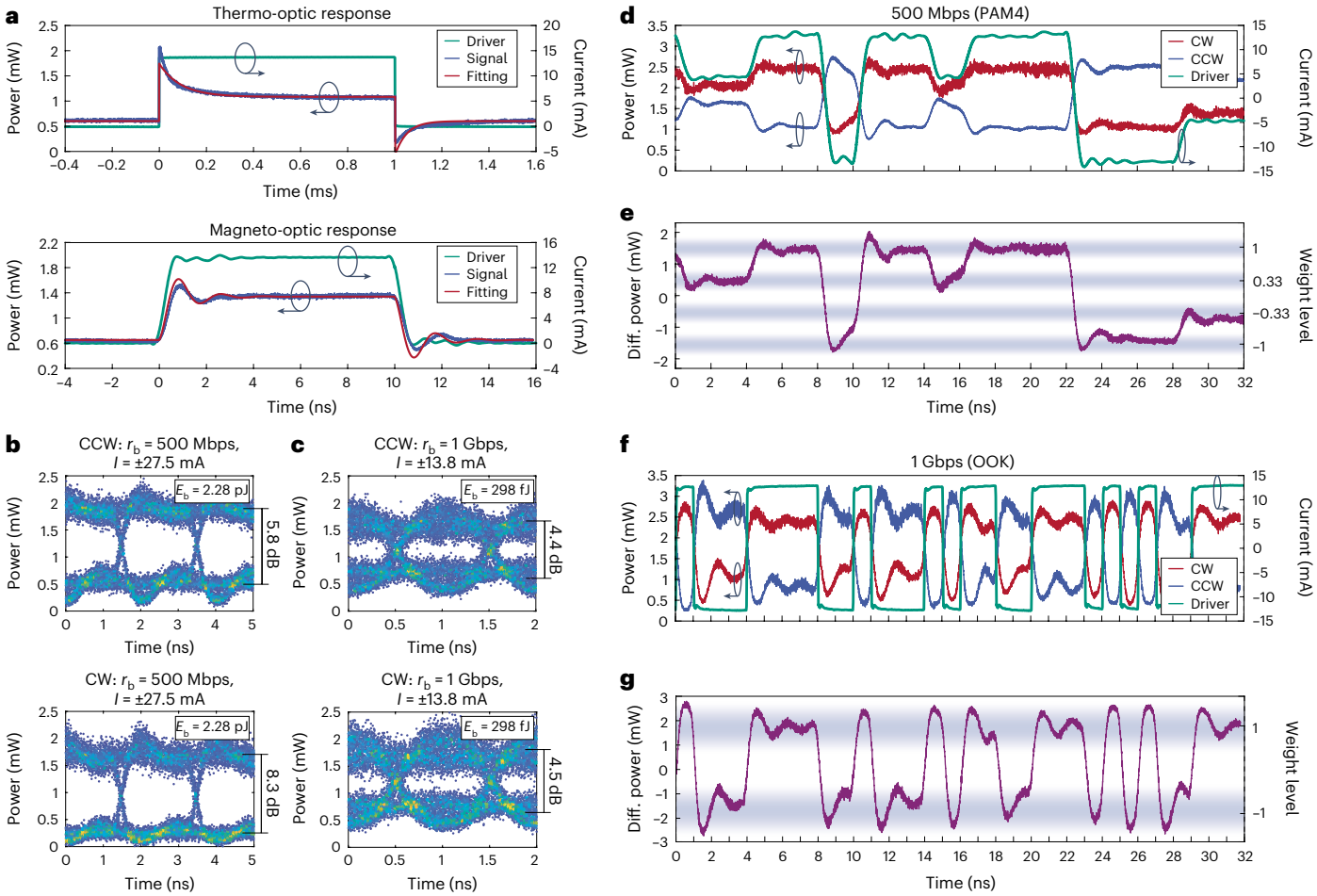

Fig. 4 | Dynamic response of non-reciprocal optical memory. a, Comparison of dynamic response of thermo- and magneto-optic effects, demonstrating a five-orders-of-magnitude difference in response time (red-detuned CW probe used for both measurements). From the thermo-optic response, the fall time is 92 µs, whereas the rise time is 50 µs. For high-speed modulation above ~1 MHz, the thermo-optic effect is negligible provided the average power dissipated remains constant. The magneto-optic response can be fit with a second-order response with a natural angular frequency of 3.6 Grad s^{-1} and a dimensionless damping factor equal to 0.29. From these results, we estimate a rise/fall time of 0.95 ns and a ferromagnetic resonance of 0.55 GHz (see Supplementary Section 3 for more details). **b**,**c**, Eye diagrams for clockwise and counterclockwise propagating modes for pseudorandom binary sequence modulation at bit rate r_b = 500 Mbps (**b**) and 1 Gbps (**c**) speeds. **d**, Simultaneous measurement of CW and CCW transmission for PAM4 modulation at 500 Mbps. Optical transmission of the CW and CCW modes are shown in red and blue, respectively, while the current applied to the electromagnet is shown in green. **e**, Plot of differential optical power between CW and CCW signals demonstrating the ability to rapidly update non-reciprocal multibit optical weights. **f**, Simultaneous measurement of CW and CCW transmission for binary modulation (on–off keying (OOK)) at 1 Gbps. **g**, Differential optical power between CW and CCW signals demonstrating programming speeds up to 1 ns.

response of the memory cell. The results in Fig. 5b show at least 11 distinct optical transmission levels corresponding to a non-volatile memory cell capable of storing ~3.5 bits; however, this value is limited by our experimental set-up rather than the device itself. In Supplementary Section 4 we provide a theoretical analysis of the magnetic, thermal and optical noise and expect the maximum bit precision of our device to exceed 13 bits.

The intermediate spectra obtained for a sweep from negative to positive current values is shown in Fig. 5c, whereas the reverse sweep from positive to negative is shown in Fig. 5d. The dashed lines in Fig. 5c,d represent the position of the optical probe used to plot the hysteresis of the through-port transmission (Fig. 5b). At this probe wavelength, we observe a maximum extinction ratio of 16.2 dB between the minimum and maximum non-volatile states. To better visualize the spectral dependence on programming current, we sequentially plot the optical transmission spectra for the full current sweep as a waterfall graph in Fig. 5e. As the current increases from negative to positive values, the MRR resonance blue shifts until saturation. Reversing the current from positive to negative values causes a red shift back to the original resonance position.

To demonstrate the ultra-high cycling endurance of our non-reciprocal memory cell, we programmed an arbitrary function generator to cycle between write and erase pulses at a rate of 10 kHz, with an amplitude of ±5 V and a pulse width of 500 ns. The optical transmission was captured manually during the three-day experiment and is shown in Fig. 5f (see Supplementary Section 2.2 for more experimental details). After 2.4 billion write and erase cycles, the device continued to function without any sign of degradation (Fig. 5g). This is a greater than three orders of magnitude improvement over past photonic memory technologies, highlighting the benefit of using optically coupled magnetic media for non-volatile data storage. Although we do see a variation in the extinction ratio of the device in Fig. 5f,g, we attribute this to slight thermal and mechanical drift of the unpackaged device during the three-day experiment. To confirm the long-term non-volatile stability of our device, we also compared the non-reciprocal spectral shift of the CW and CCW modes after programming and see

https://doi.org/10.1038/s41566-024-01549-1

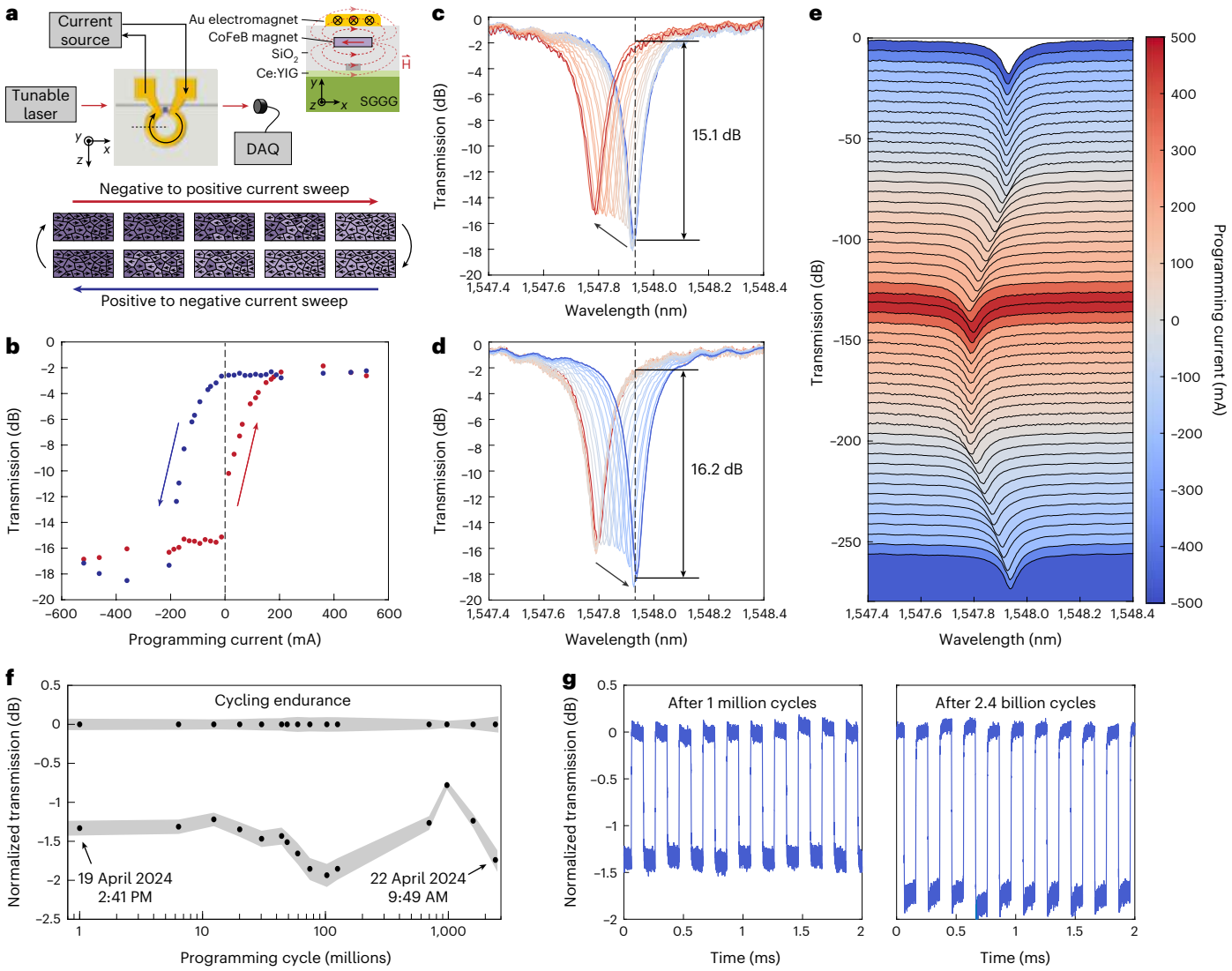

Fig. 5 | Non-volatile magneto-optic storage. a, Experimental set-up for non-volatile weight encoding. The magnetic field from the gold electromagnet aligns the magnetic domains of the CoFeB ferromagnetic layer according to the amplitude and polarity of the applied current. **b**, Hysteresis of optical transmission for a non-reciprocal memory cell with CoFeB bar magnets integrated on-chip. For these transmission measurements, the probe wavelength was fixed (black dashed lines in **c** and **d**). **c**, Negative to positive programming current sweep showing a blue shift for positive currents. **d**, Positive to negative current sweep showing a return back to the original resonance position. **e**, Waterfall plot of transmission spectra for sequential programming currents sweeping first in the positive and then in the negative directions. **f**, Demonstrated cycling endurance for over 2.4 billion write and erase cycles. Mean values of the non-volatile write and erase states are shown as black data points, whereas grey bands represent the standard deviation. Time domain measurements in **g** show the operation of the memory cell without observing any degradation. Variation in the observed extinction ratio is attributed to thermal drift of the unpackaged device over the three-day measurement.

data retention over a four-day measurement (see Supplementary Section 2.2). Opto-electronic packaging with active thermal control is expected to counter drift of the MRR resonance peak, which would address this observed variation in the extinction ratio.

Conclusion

We have demonstrated the first instance of a non-volatile magneto-optical memory cell that features non-reciprocity for in-memory computing in the optical domain. This unique combination of fast, fatigue-free programmability with non-volatile weights addresses current limitations of existing integrated approaches to optical memory that have yet to combine: (1) non-volatility, (2) multibit storage, (3) high switching speed, (4) low switching energy and (5) high endurance, in a single platform. In Table 1 we compare state-of-the-art demonstrations of various non-volatile photonic memory technologies capable of being integrated on-chip. It is worth noting that although some recent demonstrations of waveguide-integrated electronic memristors (termed memresonators) have shown great promise for fast and efficient non-volatile switching between two or three states[32,33], the maximum cycling endurance of such devices has not been demonstrated beyond 1,000 write–erase cycles. These devices are also not well suited for photonic computing applications where multi-level, non-volatile storage is necessary. Although phase-change memory has shown great promise for optical computing platforms due to its compact footprint, multi-level storage and ease of integration[15,34–36], the limited cycling endurance, high switching energies and limited switching speeds remain outstanding challenges. Other non-volatile photonic memory cells leveraging charge trapping, MEMS, or ferroelectric materials have sub-megahertz programming speeds which are not yet practical for computing applications due to considerable write latencies.

Compared with these competing photonic memory technologies, our non-reciprocal magneto-optic memory cell offers an efficient non-volatile storage solution that could provide unlimited read/write endurance at sub-nanosecond programming speeds. Our initial results used integrated electromagnets to switch a non-volatile ferromagnetic layer, however, we expect future implementations employing spin–orbit–torque or spin–torque-transfer effects could further improve the switching efficiency of our magneto-optic memory cells and provide a direct optical interface to emerging magnetic and spintronic memory technologies. Although bonding Ce:YIG on silicon-on-insulator wafer and depositing amorphous silicon on Ce:YIG are currently the best fabrication techniques for integrating high-quality Ce:YIG in silicon photonics, recent strides in the monolithic integration of magneto-optic garnet on silicon and silicon nitride substrates offer a pathway to further enhancements in the near future[37]. By precisely depositing magneto-optic materials on specific areas, we can further reduce the insertion loss and achieve higher integration density for non-reciprocal photonic computing.

Online content

Any methods, additional references, Nature Portfolio reporting summaries, source data, extended data, supplementary information, acknowledgements, peer review information; details on author contributions and competing interests; and statements of data and code availability are available at https://doi.org/10.1038/s41566-024-01549-1.

References

1. Amodei, D. & Hernandez, D. AI and compute. *OpenAI* https://openai.com/blog/ai-and-compute/ (16 May 2018).
2. Thompson, N. C., Greenewald, K., Lee, K. & Manso, G. F. *The Computational Limits of Deep Learning* Vol. 4 (MIT, 2020).
3. Mehonic, A. & Kenyon, A. J. Brain-inspired computing needs a master plan. *Nature* **604**, 255–260 (2022).
4. Rupp, K. 50 Years of Microprocessor Trend Data. *GitHub* https://github.com/karlrupp/microprocessor-trend-data (2022).
5. Shalf, J. The future of computing beyond Moore's law. *Philos. Trans. R. Soc. A* **378**, 20190061 (2020).
6. Shastri, B. J. et al. Photonics for artificial intelligence and neuromorphic computing. *Nat. Photon.* **15**, 102–114 (2021).
7. Demirkiran, C. et al. An electro-photonic system for accelerating deep neural networks. *ACM J. Emerg. Technol. Comput. Syst.* **19**, 1–31 (2023).
8. Peng, B., Hua, S., Su, Z., Xu, Y. & Shen, Y. A 64×64 integrated photonic accelerator. In *2022 IEEE Photonics Conference (IPC)* MB4.4 (IEEE, 2022).
9. Tait, A. N., Nahmias, M. A., Shastri, B. J. & Prucnal, P. R. Broadcast and weight: an integrated network for scalable photonic spike processing. *J. Lightwave Technol.* **32**, 4029–4041 (2014).
10. Shen, Y. et al. Deep learning with coherent nanophotonic circuits. *Nat. Photon.* **11**, 441–446 (2017).
11. Feldmann, J. et al. Parallel convolutional processing using an integrated photonic tensor core. *Nature* **589**, 52–58 (2021).
12. Huang, C. et al. A silicon photonic–electronic neural network for fibre nonlinearity compensation. *Nat. Electron.* **4**, 837–844 (2021).
13. Ashtiani, F., Geers, A. J. & Aflatouni, F. An on-chip photonic deep neural network for image classification. *Nature* **606**, 501–506 (2022).
14. Xu, X. et al. 11 TOPS photonic convolutional accelerator for optical neural networks. *Nature* **589**, 44–51 (2021).
15. Wu, C. et al. Programmable phase-change metasurfaces on waveguides for multimode photonic convolutional neural network. *Nat. Commun.* **12**, 96 (2021).
16. Ielmini, D. & Wong, H.-S. P. In-memory computing with resistive switching devices. *Nat. Electron.* **1**, 333–343 (2018).
17. Zhang, W. et al. Silicon microring synapses enable photonic deep learning beyond 9-bit precision. *Optica* **9**, 579–584 (2022).
18. Feldmann, J. et al. Integrated 256 cell photonic phase-change memory with 512-bit capacity. *IEEE J. Sel. Top. Quantum Electron.* **26**, 1–7 (2020).
19. Youngblood, N. Coherent photonic crossbar arrays for large-scale matrix–matrix multiplication. *IEEE J. Sel. Top. Quantum Electron.* **29**, 1–11 (2022).
20. Yang, G. et al. Processing-in-memory using optically-addressed phase change memory. In *ACM/IEEE International Symposium on Low Power Electronics and Design* (ACM, IEEE, 2023).
21. Resch, S. et al. On endurance of processing in (non-volatile) memory. In *Proc. 50th Annual International Symposium on Computer Architecture* 1–13 (ACM, 2023); https://doi.org/10.1145/3579371.3589114
22. Youngblood, N., Ríos, Ocampo, C. A., Pernice, W. H. P. & Bhaskaran, H. Integrated optical memristors. *Nat. Photon.* **17**, 561–572 (2023).
23. Pintus, P. et al. An integrated magneto-optic modulator for cryogenic applications. *Nat. Electron.* **5**, 604–610 (2022).
24. Murai, T., Shoji, Y., Nishiyama, N. & Mizumoto, T. Non-volatile magneto-optical switches integrated with a magnet stripe array. *Opt. Express* **28**, 31675 (2020).
25. Shoji, Y., Taniguchi, S. & Yajima, S. Non-volatile photonic switch with magnetic materials on a silicon photonic platform [Invited]. *Opt. Mater. Express* **13**, 2489 (2023).
26. Tait, A. N. et al. Microring weight banks. *IEEE J. Sel. Top. Quantum Electron.* **22**, 312–325 (2016).
27. Pintus, P. Accurate vectorial finite element mode solver for magneto-optic and anisotropic waveguides. *Opt. Express* **22**, 15737–15756 (2014).
28. Onbasli, M. C. et al. Optical and magneto-optical behavior of Cerium Yttrium Iron Garnet thin films at wavelengths of 200–1770 nm. *Sci Rep.* **6**, 23640 (2016).
29. Zaets, W. & Ando, K. Optical waveguide isolator based on nonreciprocal loss/gain of amplifier covered by ferromagnetic layer. *IEEE Photon. Technol. Lett.* **11**, 1012–1014 (1999).
30. Freeman, M. R. Picosecond pulsed-field probes of magnetic systems (invited). *J. Appl. Phys.* **75**, 6194–6198 (1994).
31. Rey-De-Castro, R. et al. Subpicosecond Faraday effect in $Cd_{1-x}Mn_xTe$ and its application in magneto-optical sampling. *Appl. Phys. Lett.* **85**, 3806–3808 (2004).
32. Tossoun, B. et al. High-speed and energy-efficient non-volatile silicon photonic memory based on heterogeneously integrated memresonator. *Nat. Commun.* **15**, 551 (2024).
33. Fang, Z. et al. Fast and energy-efficient non-volatile III–V-on-silicon photonic phase shifter based on memristors. *Adv. Opt. Mater.* **11**, 2301178 (2023).
34. Ríos, C. et al. In-memory computing on a photonic platform. *Sci. Adv.* **5**, eaau5759 (2019).
35. Zhou, W. et al. In-memory photonic dot-product engine with electrically programmable weight banks. *Nat. Commun.* **14**, 2887 (2023).
36. Feldmann, J., Youngblood, N., Wright, C. D., Bhaskaran, H. & Pernice, W. H. P. All-optical spiking neurosynaptic networks with self-learning capabilities. *Nature* **569**, 208–214 (2019).
37. Zhang, Y. et al. Monolithic integration of broadband optical isolators for polarization-diverse silicon photonics. *Optica* **6**, 473–478 (2019).
38. Song, J.-F. et al. Integrated photonics with programmable non-volatile memory. *Sci Rep.* **6**, 22616 (2016).
39. Edinger, P. et al. A bistable silicon photonic MEMS phase switch for non-volatile photonic circuits. In *2022 IEEE 35th International Conference on Micro Electro Mechanical Systems Conference (MEMS)* 995–997 (IEEE, 2022); https://doi.org/10.1109/MEMS51670.2022.9699739

40. Taki, K. et al. Non-volatile optical phase shift in ferroelectric hafnium zirconium oxide. *Nat. Commun.* **15**, 3549 (2023).
41. Geler-Kremer, J. et al. A ferroelectric multilevel non-volatile photonic phase shifter. *Nat. Photon.* **16**, 491–497 (2022).
42. Fang, Z. et al. Ultra-low-energy programmable non-volatile silicon photonics based on phase-change materials with graphene heaters. *Nat. Nanotechnol.* **17**, 842–848 (2022).
43. Emboras, A. et al. Atomic scale plasmonic switch. *Nano Lett.* **16**, 709–714 (2016).

Methods

The transmission spectra of magneto-optic memory cell in Fig. 3 is modelled using the transfer matrix method, in which the effective index of the CW and CCW modes is computed using a finite-element method. The resonance of the MRR is controlled by the current in the integrated electromagnet, giving rise to a magnetic field and a Joule heating effect. The magneto- and thermo-optic effects alter the effective index of the modes, and their impact is described using a perturbative approach. A comprehensive description of the model employed is provided in Supplementary Section 1.

To fabricate the magneto-optic material used for all devices, a 500-nm-thick single-crystalline Ce:YIG ($Ce:Y_2Fe_5O_{12}$) was epitaxially grown on a wafer of (111)-oriented (Ca, Mg, Zr) SGGG using an radio frequency sputtering method at 750 °C. This magneto-optic garnet has a large Faraday rotation of 4,800 degrees per centimetre at 1,550 nm and was used for all of the devices presented in this work.

The devices characterized in Figs. 3 and 4 were fabricated by bonding a Ce:YIG/SGGG on a 220-nm-thick SOI wafer with 2 µm buried oxide. The SOI wafer is patterned using a 248 nm ASML 5500 deep-ultraviolet stepper, and dry etched using a Bosch process (Plasma-Therm 770) to form the waveguides and resonators. Patterned SOI and Ce:YIG/SGGG samples are rigorously cleaned, and activated with O_2 plasma (EVG 810). Ce:YIG is directly bonded onto the SOI wafer using a flip-chip bonder (Finetech) and then annealed at 200 °C for 6 h under 3 MPa to strengthen the bond. The required alignment accuracy is fairly tolerant (~200 µm). After bonding, a 1 µm layer of SiO_2 is sputtered everywhere on the chip as an upper cladding. The SGGG substrate is then thinned by mounting the sample against a flat chuck and polishing (Allied Technologies) using a series of increasingly fine lapping films. The thickness of SGGG is monitored using a micrometre and confirmed to be ~5 µm with a separate Dektak profilometry measurement. The variation of thickness across the sample is roughly ±1.5 µm due to imperfect levelling of the chuck. The patterns for gold coils and contacts are defined on the backside of the SGGG with a 365 nm GCA i-line wafer stepper. Then, using electron-beam evaporation, 22 nm of titanium is deposited as an underlayer, followed by 1.5 µm of gold, and the metal coils and contacts are released by a lift-off procedure. Finally, the sample is diced and the facets are polished.

Non-volatile magneto-optic memory cell characterized in Fig. 5 is fabricated growing amorphous silicon (a-Si) on a Ce:YIG/SGGG wafer. A 10-nm-thick SiO_2 buffer layer is deposited onto a Ce:YIG/SGGG wafer via plasma-enhanced chemical vapour deposition (PE-CVD). Next, a 220-nm-thick a-Si:H guiding layer is deposited via PE-CVD with a gas mixture of SiH_4 at 300 °C. Subsequently, a 200-nm-thick SiO_2 layer is deposited as a hard mask to protect the a-Si:H layer, and a 300-nm-thick positive resist (ZEP-520A), as well as a charge-dissipating agent (ESPACER), are coated onto the substrate. Waveguide patterns are exposed to the resist using an electron-beam lithography system. The waveguide patterns are transferred to a SiO_2 hard mask via reactive ion etching using CF_4 and a-Si:H waveguides are formed using SF_6. A 750-nm-thick SiO_2 layer is deposited on the top of the waveguide core to isolate the guided mode from the integrated thin-film magnet to avoid optical absorption. Electron-beam lithography is performed to transfer the magnet patterns of an array of 20 µm × 5 µm stripes. A 10-nm-thick ruthenium buffer layer followed by a 300-nm-thick CoFeB thin-film magnet are deposited using an radio frequency facing target sputtering method at room temperature with argon. Next, the stripe array of thin-film magnets is formed using the lift-off process. The longer side of each stripe, which is the easy magnetization axis of CoFeB, is aligned perpendicular to the waveguide. Finally, after the deposition of an 80-nm-thick SiO_2 layer using PE-CVD, a 25-µm-wide and 700-nm-thick Cr/Au electromagnet for magnetizing integrated magnets was formed via electron-beam vapour deposition.

Data availability

Data sets generated during the current study are available from the corresponding author on reasonable request.

Code availability

The complete simulation code and all simulation files required to reproduce the results presented in Fig. 2 is available at https://nonreciprocalringresonators.github.io.

Acknowledgements

N.Y. acknowledges support from the US National Science Foundation under (grant nos. ECCS-2210168/2210169 and CISE-2105972). N.Y. acknowledges support from the University of Pittsburgh Center for Research Computing (grant no. RRID:SCR_022735) via the resources provided. Specifically, this work used the H2P cluster, which is supported by NSF award no. OAC-2117681. P.P., G.M. and J.E.B. acknowledge support from the Air Force Office of Scientific Research under award nos. FA9550-21-1-0042 and FA9550-20-1-0150. P.P. also acknowledges support from the Autonomous Region of Sardinia via the 'Mobilità Giovani Ricercatori (MGR)' programme of the University of Cagliari; the Italian Ministry of University and Research via the PRIN PNRR 2022 project 'Magneto-optic Integrated Computing (MAGIC)' (grant no. CUP F53D23008340001); and the Fondazione di Sardegna via the 'Investigation of Novel Magneto-Optic Materials and Devices for Silicon Photonic Integrated Circuits' project (grant no. CUP F73C23001820007). Any opinions, findings and conclusions or recommendations expressed in this material are those of the authors and do not necessarily reflect the views of the US Air Force.

Author contributions

N.Y. and P.P. conceived the idea and the experiments. N.Y., P.P., G.M. and J.E.B. oversaw the data collection. T.M., Y.S. and D.H. fabricated the devices. Y.S. grew the Ce:YIG thin films used in device fabrication. V.S. and P.P. performed mathematical modelling and numerical simulations of the devices. P.P., M.D., Y.S. and T.M. performed optical characterization of fabricated devices. N.Y. and P.P. wrote the manuscript with input and feedback from all of the authors.

Competing interests

The authors declare the following competing interests: N.Y. and P.P. have filed a patent application related to this work. The other authors declare no competing interests.

Additional information

Supplementary information The online version contains supplementary material available at https://doi.org/10.1038/s41566-024-01549-1.

Correspondence and requests for materials should be addressed to Paolo Pintus or Nathan Youngblood.

Peer review information *Nature Photonics* thanks Yang Chai and Bert Offrein for their contribution to the peer review of this work.

nature photonics

Supplementary information

https://doi.org/10.1038/s41566-024-01549-1

Integrated non-reciprocal magneto-optics with ultra-high endurance for photonic in-memory computing

In the format provided by the authors and unedited

Index

1. Mathematical modelling of nonreciprocal magneto-optic memory cell

To compute the transfer function of a memory cell, we developed a mathematical model based on the 2.5D electromagnetic mode analysis [1], including the magneto-optic and thermo-optic effects a perturbation on the effective index [2], [3].

When no current is injected into the electromagnet (no magnetic field), the electrical permittivity of all the materials in the device is isotropic. Under those conditions, we computed the optical mode of the waveguide shown in Figure S1.

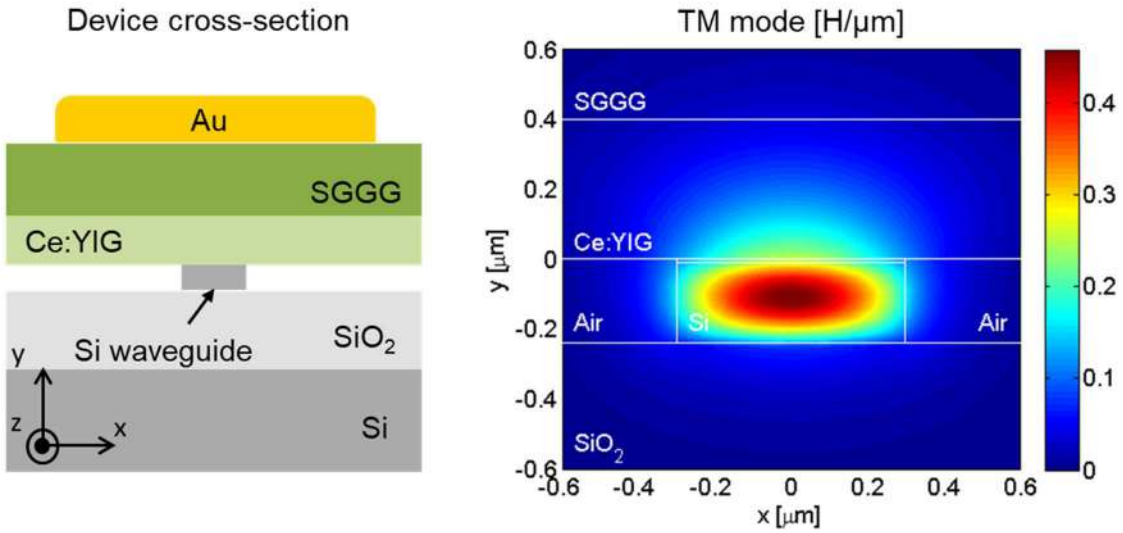

Figure S1: Cross-section of the device with an integrated Au electromagnet (left), and profile of the transverse magnetic (TM) optical mode in the silicon/Ce:YIG waveguide (right). For the TM mode we show the main component of the magnetic field.

Injecting a current in the electromagnet produces an in-plane magnetic field and a local variation of the temperature (Joule heating), resulting in a phase change and optical absorption variation of the optical mode that propagates in the waveguide. We can distinguish two contributions of the phase change: a reciprocal term that depends on the temperature (thermo-optic effect), and a nonreciprocal one that depends on the magnetic field (magneto-optic nonreciprocal phase shift effect [4]). The magnetic field also induces a nonreciprocal variation in the propagation loss depending on the field intensity and the direction of light propagation (magneto-optic nonreciprocal loss effect [2], [5]). Due to the small dimension of the waveguide compared to the scale of variation of the magnetic field and the temperature distribution, the effective index and the propagation loss of the optical mode can be written as

$$n_{\mathrm{eff}} = n_{\mathrm{eff}}^{0} + \Delta \mathrm{n}_{\mathrm{TO}} + \Delta \mathrm{n}_{\mathrm{MO}} \tag{1}$$

$$\alpha_{\mathrm{eff}} = \alpha_{\mathrm{eff}}^{0} + \Delta \alpha_{\mathrm{MO}} \tag{2}$$

where n_{eff}^{0} and $\alpha_{\mathrm{eff}}^{0}$ are the effective index and the propagation loss of the mode in the unperturbed case, respectively; $\Delta \mathrm{n}_{\mathrm{TO}}$ is the variation of the effective index induced by the temperature, while $\Delta \mathrm{n}_{\mathrm{MO}}$ and $\Delta \alpha_{\mathrm{MO}}$ are the nonreciprocal variation of the effective index and propagation loss produced by the magnetic field in the MO material.

1.1. Thermo-optic effect

The thermo-optic phase shift is computed combining the results of a multi-physics simulation software with the outcomes of the mode analysis. The variation of the effective index of the mode with respect to the temperature is calculated with the following expression:

$$\Delta n_{\mathrm{TO}} = \frac{dn_{\mathrm{eff}}}{dT}\Delta T = \left[\frac{dn_{\mathrm{eff}}}{dn_{\mathrm{Si}}}\frac{dn_{\mathrm{Si}}}{dT} + \frac{dn_{\mathrm{eff}}}{dn_{\mathrm{SiO2}}}\frac{dn_{\mathrm{SiO2}}}{dT} + \frac{dn_{\mathrm{eff}}}{dn_{\mathrm{CeYIG}}}\frac{dn_{\mathrm{CeYIG}}}{dT} + \frac{dn_{\mathrm{eff}}}{dn_{\mathrm{Air}}}\frac{dn_{\mathrm{Air}}}{dT}\right]\Delta T \qquad (3)$$

where dn_i/dT is the thermo-optic coefficient of the material (i=Si, SiO_2, Ce:YIG and air) that can be find in the literature (see supplementary material of [6]), while dn_{eff}/dn_i is a function of the waveguide geometry and are computed using the mode analysis. The temperature variation is computing using COMSOL Multiphysics [7] and it is almost constant in the area that overlaps 99% of the optical mode.

1.2. Magneto-optic effect

Similar to the previous section, the phase shift and propagation loss induced by the magnetic field (nonreciprocal effect) is obtained combining the magnetic field generated by the electromagnet and computed with COMSOL with the results of an electromagnetic mode solver for magneto-optic waveguides developed in-house [2].

At the optical frequencies, the electrical permittivity of a MO material is modified by the magnetic field produced by the electromagnet [8]. In the case under investigation, the magnetic field is directed along the x-axis (reference frame in Figure S1), such that the permittivity tensor of the Ce:YIG above the silicon waveguide becomes

$$\varepsilon_r = \begin{pmatrix} \varepsilon_{xx} & 0 & 0 \\ 0 & \varepsilon_{yy} & j\varepsilon_{yz} \\ 0 & -j\varepsilon_{yz} & \varepsilon_{zz} \end{pmatrix} \qquad (4)$$

in the tensor $\varepsilon_{xx} = \varepsilon_{yy} = \varepsilon_{zz} = (n_{\mathrm{Ce:TIG}} + i\kappa_{\mathrm{Ce:YIG}})^2$, where $n_{\mathrm{Ce:YIG}}$ and $\kappa_{\mathrm{Ce:YIG}}$ are the real and imaginary part of the optical refractive index.

The nonreciprocal optical properties of the Ce:YIG are induced by the presence of an external magnetic field and are modelled through the off-diagonal terms ε_{yz} in Eq. (4). When the real part of ε_{yz} is not null, we observe a non-reciprocal phase shift (NRPS) for the transverse magnetic (TM) mode, while the transverse electric (TE) mode remains unaffected. In a complementary manner, when the imaginary part of ε_{yz} is not zero, the propagation loss of the TM mode differs for the forward and backward propagating direction, resulting in a nonreciprocal loss (NRL) while the loss of the TE mode remains unchanged.

If the in-plane magnetic field is larger than 50 Oe (5 mT), the magnetization of the Ce:YIG saturates. Under this condition, the real part of ε_{yz} is related to the Faraday rotation constant θ_F^0 by the following expression:

$$\mathbb{R}e\{\varepsilon_{yz}\} = \frac{2n_{\mathrm{Ce:YIG}}\theta_F^0}{k_0} \qquad (5)$$

where k_0 is the propagation constant (or the wavenumber) in the vacuum and θ_F^0=4500°/cm, resulting in $\mathbb{R}\mathrm{e}\{\varepsilon_{yz}\}$=8.6·10^{-3}. For the imaginary part of ε_{yz} we used the value reported in the literature at 1550 nm for the (111)-oriented Ce:YIG, which is $\mathbb{I}\mathrm{m}\{\varepsilon_{yz}\}$=7.33·10^{-5}, [9].

Figure S2 shows the effective index of the TM optical mode in the range between 1540 nm and 1560 nm, computed when the Ce:YIG is magnetically saturated. As we can observe from the numerical results, the effective index for the forward propagating mode, n_{eff}^{+}, and the backpropagating mode, n_{eff}^{-}, results differentiated. As a reference, we also plotted n_{eff} which is the value of the effective index in the case when the term ε_{yz} are null. Similar results are obtained for the propagation loss $\alpha_{\mathrm{eff}}^{\pm} = 22 \pm 3.5$ dB/cm, where the sign depends on the propagating direction.

The geometry that maximizes the NRPS effect for the TM mode requires a 600 nm wide and 220 nm tall silicon waveguide with a 400 nm thick Ce:YIG on top. The mode analysis shown in Figure S1 and the effective indices in Figure S2 refer to this case. In the mode analysis we have also included a 10-nm oxide layer between the silicon waveguide and the Ce:YIG. This layer is a byproduct of the bonding process and reduces the largest NRPS achievable in this geometry [10].

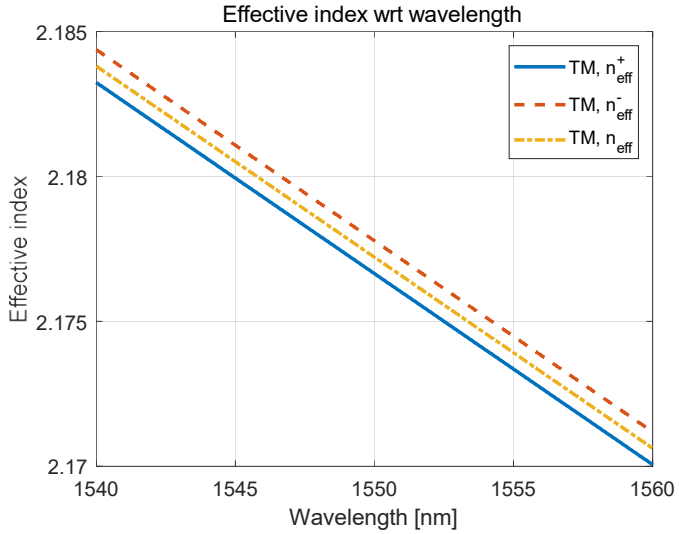

Figure S2: Effective index of the TM mode versus wavelength. When no magnetic field is applied, the effective index is 2.177 at 1550 nm. Above magnetic saturation, it changes by ±5.66·10^{-4} with respect to the two directions. The group index (n_g = 3.199) does not change significantly amongst the three cases.

Below magnetic saturation (<50 Oe), the Faraday rotation does not reach its largest value and the effective index variation due to the magneto-optic effect decreases. Since the off-diagonal terms are small when compared to the diagonal entries of the permittivity tensor, we can treat the case using a linear approximation:

$$\Delta \mathrm{n}_{\mathrm{MO}} = \Delta \mathrm{n}_{\mathrm{MO}}^{sat} \frac{\theta_F}{\theta_F^0} \tag{6}$$

where $\Delta \mathrm{n}_{\mathrm{MO}}^{sat}$ is the largest refractive index variation when the Ce:YIG is magnetically saturated, and θ_F is the Faraday rotation measured below saturation. The value of θ_F increases linearly with the magnetic field until it reaches a saturation value, while it decreases linearly when the temperature rises. A simple model is:

$$\theta_F(H_x, T) = \left[\theta_F^0 + \frac{d\theta_F}{dT}(T - T_{amb})\right] \cdot \tanh\frac{H_x}{H_x^0} \tag{7}$$

where H_x is the in-plane magnetic field, H_x^0 is a constant, T is temperature, T_{amb} is the ambient temperature, and θ_F^0 is the Faraday rotation constant at room temperature when the material is saturated. For the Ce:YIG, the value of the constants in Eq. (7) are $\theta_F^0 = -4500^\circ/cm$, $H_x^0 = 24\ Oe$, $d\theta_F/dT = 44^\circ/K \cdot cm$ [10].

Similarly, the nonreciprocal loss below saturation can be approximated as:

$$\Delta\alpha_{\mathrm{MO}} = \Delta\alpha_{\mathrm{MO}}^{\mathrm{sat}} \cdot \tanh\frac{H_x}{H_x^0} \tag{8}$$

where $\Delta\alpha_{\mathrm{MO}}^{\mathrm{sat}}$ is the largest NRL variation under saturation.

1.3. Numerical results

Using the COMSOL Multiphysics software, we simulated the local heat and the in-plane magnetic field at the silicon/Ce:YIG waveguide. The corresponding results are shown in **Error! Reference source not found.**.

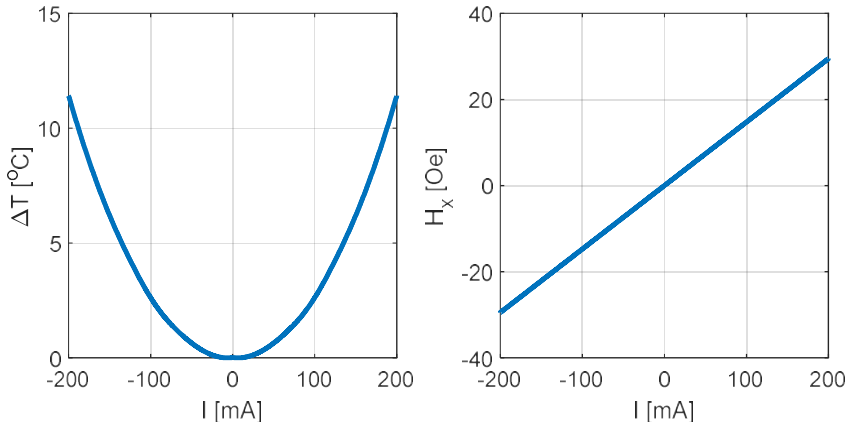

Figure S3: Temperature variation (left panel) and in-plane magnetic field (right panel) produced by the electrical current in the integrated electromagnet.

By integrating the outcomes of the thermal and magnetic field simulations with the model outlined in subsections 1.1 and 1.2, we calculate the variations of the effective index resulting from the thermo-optic and magneto-optic effects as a function of the current applied to the electromagnet. The corresponding variation of the effective index and the propagation loss are shown in Figure **S4**.

The refractive index variation for both the thermo-optic and magneto-optic effects is computed for both forward and backward propagating modes. The thermo-optic effect is reciprocal, affecting the propagating and counter-propagating modes in the same manner. Since the local heating reduces the maximum NRPS, we have also reported the maximum achievable magneto-optic refractive index variation in the scenario where no thermal heat is produced (e.g., with a permanent magnet).

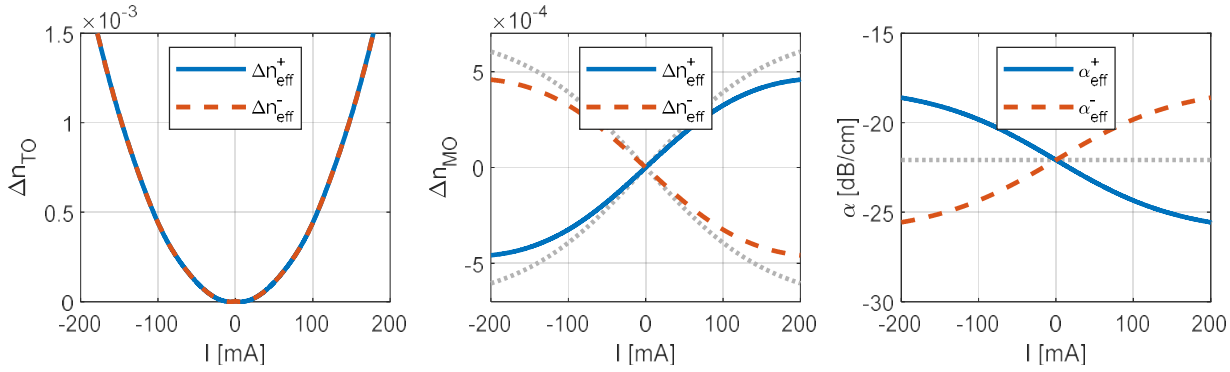

Figure S4: Refractive index variation due to the thermo-optic (left panel) and the magneto-optic effect (central panel) for the TM mode at λ=1550 nm. The dotted gray lines in the central panel show the maximum achievable NRPS in the case there is no local heating. Propagation losses for both forward and backward propagating waves are displayed in the right panel. In this instance, the dotted gray curve serves as a reference for reciprocal loss.

In the right panel of Figure **S4**, we also present the nonreciprocal propagation loss as a function of the propagation direction and the current in the electromagnet. Such a nonreciprocal loss results in a variation of the full-width at half maximum for the microring resonator, as detailed in the manuscript.

1.4. Bending loss and minimum ring radius

The minimum ring radius of the device is determined by considering the loss induced by waveguide bending. Figure S7 depicts the simulated bending loss for both TE and TM modes as a function of the curvature radius. Two critical parameters are varied: the thickness of the bonding oxide layer (left panel of Figure S7) and the width of the silicon waveguide (left panel of Figure S7). It is worth mentioning that these values serve as a lower bound since the simulations do not include the roughness of the waveguide. For our device, we assume a safe value of ring radius larger than 25 µm.

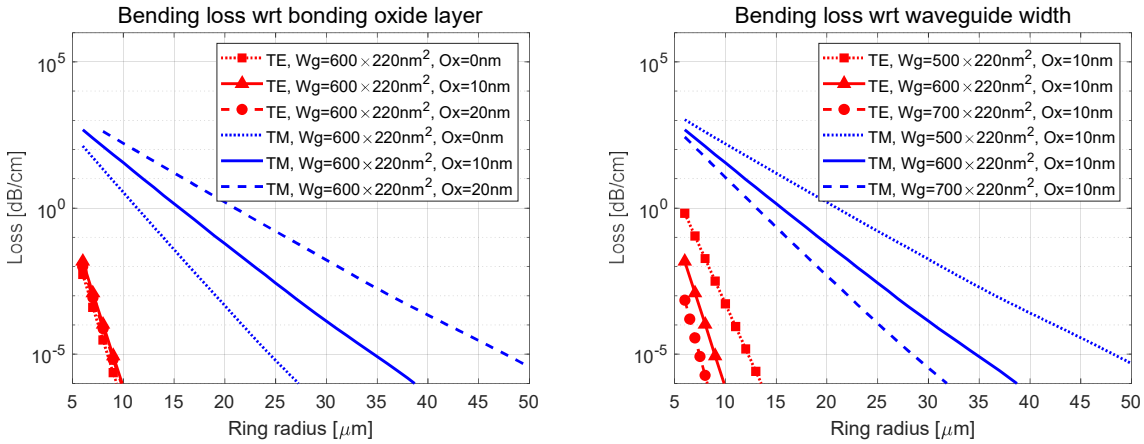

Figure S5: Bending losses for TE and TM modes at λ=1550 nm. The losses are depicted as a function of the microring radius for various waveguide configurations. In the left panel, we illustrate the bending loss of the microring when the thickness of the oxide layer varies by ±10 nm around the nominal value of 10 nm. In the right panel, the analysis of the bending losses is shown, assuming a variation of ±100 nm in the silicon waveguide width around the nominal value of 600 nm.

1.5. Microring-waveguide power coupling coefficient

In an all-pass ring resonator, a straight waveguide positioned adjacent to the microring is used to couple the optical signal in and out of the resonant cavity. To achieve the maximum excitation ratio (i.e., the largest weight contrast in the magneto-optic memory), the round-trip loss must be compensated by the power coupled into the cavity. To achieve this goal, we optimize the distance between the microring and the waveguide.

Figure S6 shows the power coupling ratio (K) between the microring and the waveguide, computed using the finite-difference time-domain method implemented in ANSYS/Lumerical. The power coupling ratios are computed assuming a ring radius of 35 μm and sweeping the microring-waveguide gap from 200 nm to 300 nm. The results shown in the figure are calculated in the reciprocal case, with no significant variation observed in the nonreciprocal condition. While the simulated power coupling ratio varies with respect to the wavelength, within the tuning range produced by the non-reciprocal phase shift (i.e., ±0.290 nm), the coupling can be assumed constant.

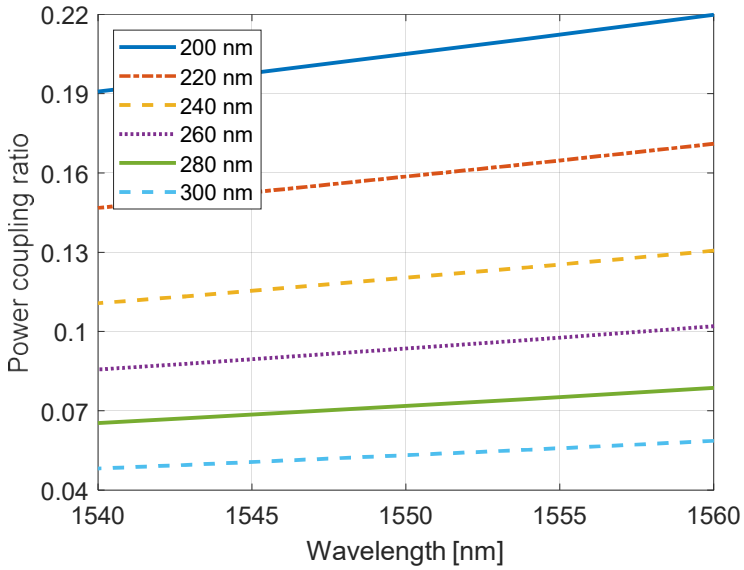

Figure S6: Power coupling ratio between the microring and the waveguide computed as a function of the wavelength for different gaps. The results refer to the case of a microring with a ring radius of 35 μm. The critical coupling condition is reached when the power coupling ratio matches the round-trip loss 0.12.

When no magnetic field is applied (reciprocal case), the propagation loss of the TM mode is expected to be 22 dB/cm, as previously shown in Figure **S4** and reported in ref. [11]. This value corresponds to a round-trip loss of $\gamma = 0.12$. In an all-pass ring resonator, the critical coupling condition is achieved when the power coupling ratio matches this loss (e.g., $K = \gamma$). At λ=1550 nm, this condition is obtained when the distance between the microring and the waveguide is approximately 250 nm. To compensate for potential variations during the fabrication process, similar devices have been fabricated with gaps ranging from 200 nm to 270 nm.

1.6. Device transfer function

In this section, we derive the input-output transfer function of the magneto-optic memory cell using the effective index for the two propagating directions. In the case of an all-pass ring resonator, such as the one investigated in the manuscript, the transfer function is:

$$T^{\pm}(\lambda, I) = e^{i(\pi+\phi^{\pm})} \frac{a^{\pm} - re^{-i\phi^{\pm}}}{1 - ra^{\pm}e^{-i\phi^{\pm}}} \tag{9}$$

where $\phi^{\pm} = n_{\text{eff}}^{\pm}(\lambda)\, k_0 L$ is the accumulated phase of a single pass for the CW $[n_{\text{eff}}^{+}(\lambda)]$ and CCW $[n_{\text{eff}}^{-}(\lambda)]$ mode in the microring, with L being the round-trip length (i.e., the microring circumference). The constant $a^{\pm} = e^{-\alpha^{\pm} L}$ is the single-pass field amplitude transmission where $\alpha^{\pm}$ is the field propagation loss for the two directions, as shown in Figure **S4** [11]. The coefficient r is the field transmission coefficient at the microring-bus section [12], [13]. If K is the power coupling ratio, $r = \sqrt{1-K}$, [14]. The amplitude and phase of the transfer functions for the CW and CCW modes are plotted in Figure S7. As a reference, we also plot the case of no magnetic field. The small variation of the extinction ratios and the full width at half maximum of the three spectra are due to the nonreciprocal loss.

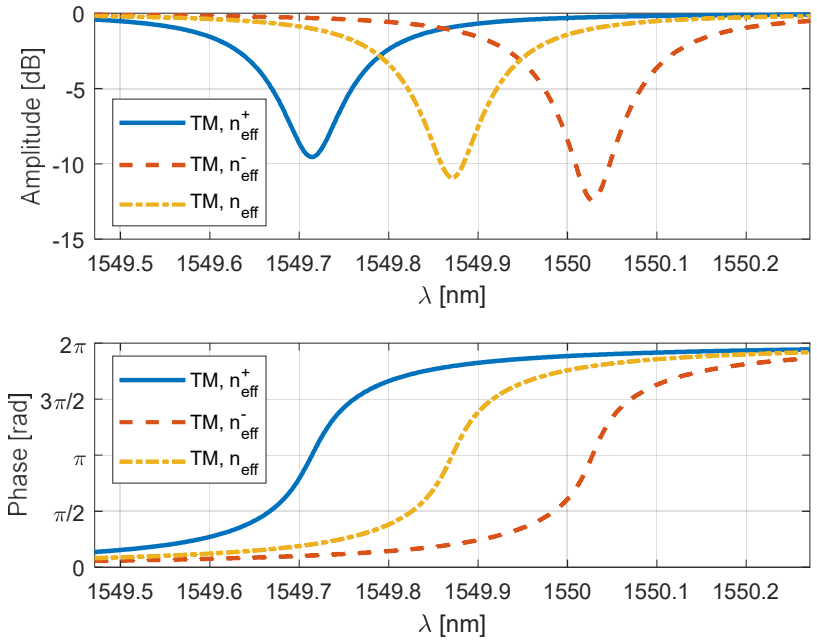

Figure S7. Amplitude and phase of the transfer function are depicted for the CW mode $[n_{\text{eff}}^{+}(\lambda)]$ and CCW *mode* $[n_{\text{eff}}^{-}(\lambda)]$ in the microring when the current in the electromagnet is set to 100 mA. The case with no current is also shown for reference $[n_{\text{eff}}(\lambda)]$

In Eq. (9), we emphasize the dependence of the transfer function on the wavelength, λ, and electrical current in the electromagnet, I, which generates the magnetic field and local heating. The encoded weight shown in Figure 2(d) and Figure 3(e) of the manuscript are defined as

$$w(\lambda, I) = T^{-}(\lambda, I) - T^{+}(\lambda, I) \tag{10}$$

1.7. Reciprocal and non-reciprocal microring resonator simulation

The simulations presented in Figure 2 of the manuscript were performed using Lumerical Interconnect on the University of Pittsburgh for Research Computing cluster nodes. In these simulations, the non-reciprocal phase shift $\phi^{\pm}$ was modeled using two reciprocal phase shift elements (one for the CW and one for the CCW propagating modes) which were addressed through two lossless circulators (see Figure S8a). Figure S8 shows the schematic diagrams of the non-reciprocal and reciprocal devices, respectively, as modeled in Lumerical Interconnect. Effects such as temperature variations and fabrication errors were not included in these simulation models.

Lumerical script files were created using Python to perform parametric sweeps by varying the coupling coefficient from 0 to 0.2, wavelength from 1545 nm to 1555 nm, and phase shift from $-\pi$ to π. The full simulation dataset was then compiled and compressed using Python libraries for efficient data management.

The complete simulation code and all simulation files required to reproduce the results presented in this chapter is available at https://nonreciprocalringresonators.github.io

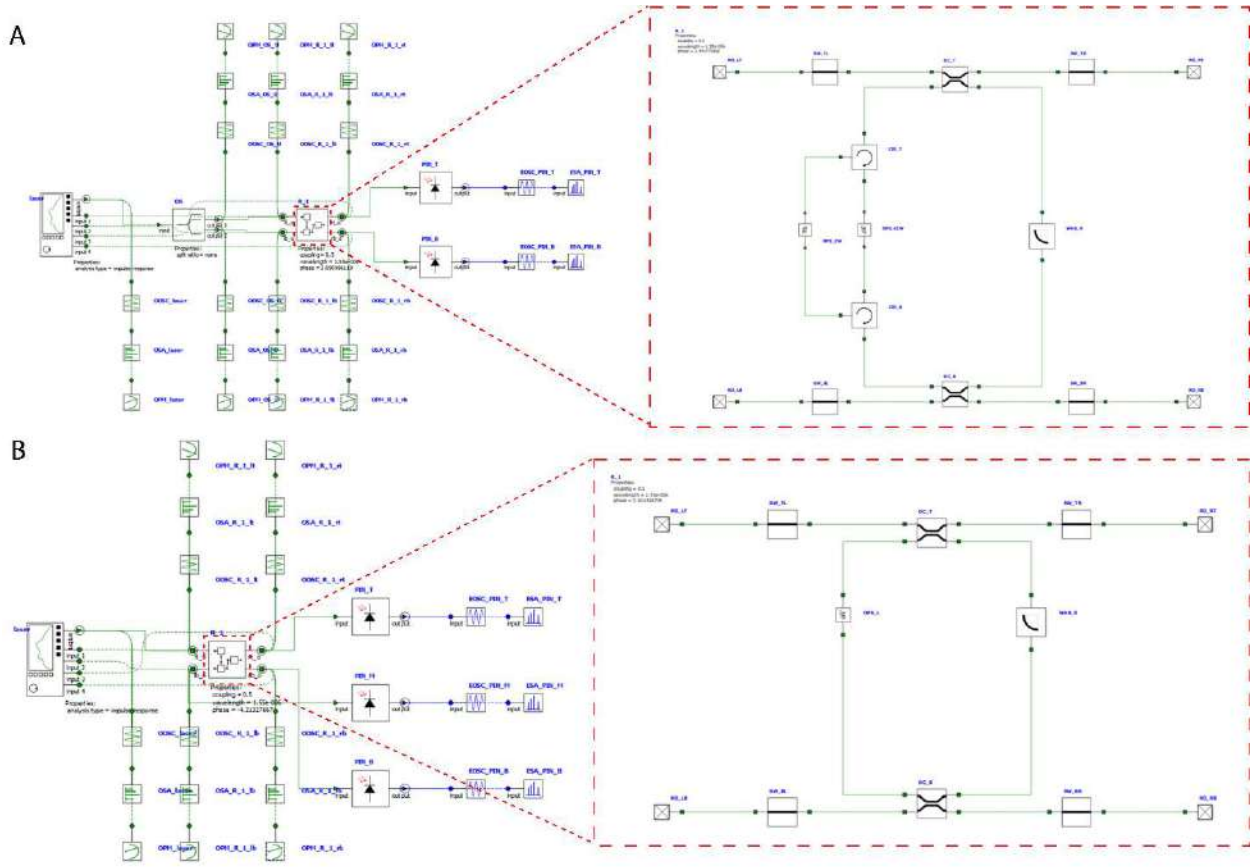

Figure S8. a) Modeling of the non-reciprocal photonic computational memory cell. The non-reciprocal phase shift is modeled using two circulators and two reciprocal phase shift elements with opposite signs. b) Modeling of reciprocal computational memory cell which uses the difference between the through and drop ports of an add-drop microring resonator to encode weight values.

2. Experimental characterization of magneto-optic memory cell

2.1. Dynamic non-reciprocal microring resonator response

In this section, we provide a detailed description of the measurement setup used to characterize the dynamic behavior of the magneto-optic memory cell. The setup configuration is shown schematically in Figure S9. The laser light, emitted from a tunable laser source (Keysight 81608A), is divided using a 50:50 directional coupler into two paths and then coupled to the two side of the chip through two lensed fibers. This configuration allows us to simultaneously excite the clockwise (CW) and the counterclockwise (CCW) modes of the microring. In each path, a circulator is employed to redirect the modulated light from the magneto-optic memory cell to a digital communication analyzer. Because the performance of the device is polarization sensitive, all fiber components in the setup are chosen to be polarization maintaining (i.e., the lensed fibers, the circulators, and the directional coupler). The lensed fibers have been carefully oriented to selectively excite only the TM-polarized mode in the waveguides with a polarization extinction ratio larger than 23 dB.

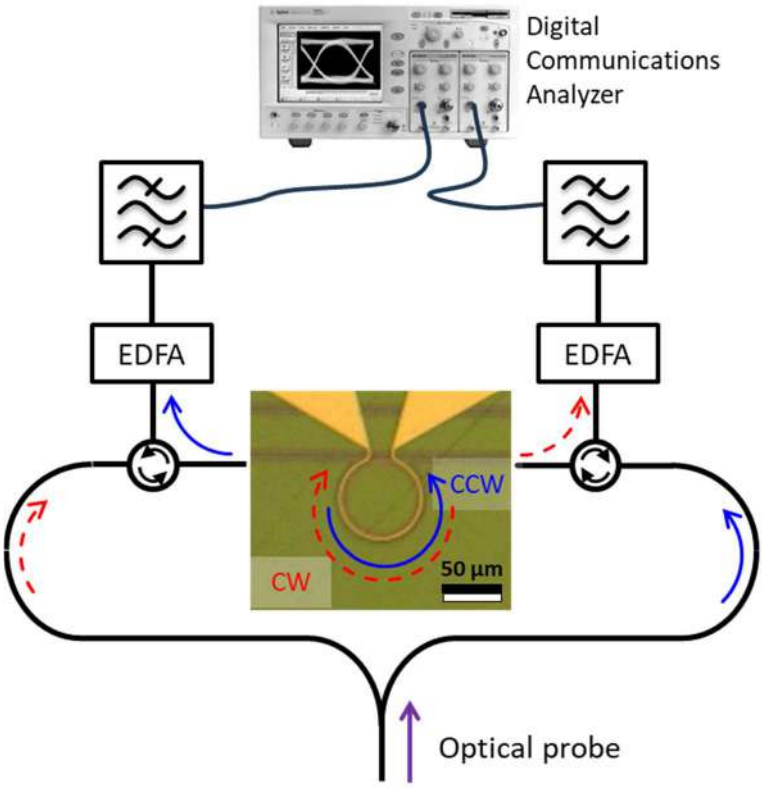

Figure S9. Measurement set-up for high-speed characterization.

The CW and CCW modulated signals coming from the chip are amplified using two erbium doped fiber amplifiers (EDFA) with similar performance (Amonics AEDFA-PA-35-B-FA and AEDFA-CL-PA-35-B-FA) and filtered using two tunable optical filters.

For the eye diagram measurements, the laser wavelength is held fixed at the full width half-maximum (FWHM) of one of the resonances. The binary modulation (On-Off Keying) at 1 Gbps

is generated using an error performance analyzer (Hewlett Packard 70843A), while the 4-level pulse amplitude modulation (PAM4) is produced using an arbitrary waveform generator (Keysight 81180B). The modulated light signals are detected using a digital communication analyzer (Agilent Infiniium DCA-J 86100C).

2.2. Characterization of memory stability and endurance

Since the optical response of the device is dependent on the magnetic field, the long-term stability of our memory cell primarily depends on the magnetization stability of the patterned CoFeB magnets integrated near the ring. CoFeB is well known for long-term storage in magnetic memory, such as MTJ-based MRAM, with predicted retention times up to 10 years [15]. To show nonvolatile data retention in our device, we have performed additional spectral measurements at time intervals for up to 4 days after switching the magnetization state (Figure S10). Since the devices are not packaged or thermal stabilized, these measurements over longer periods show minor thermal drift of the resonance position. However, when we compare the relative resonance shift of the CW and CCW modes, we can see good stability over the measurement period. We aim to explore the limits of nonvolatile stability in packaged devices in a future work.

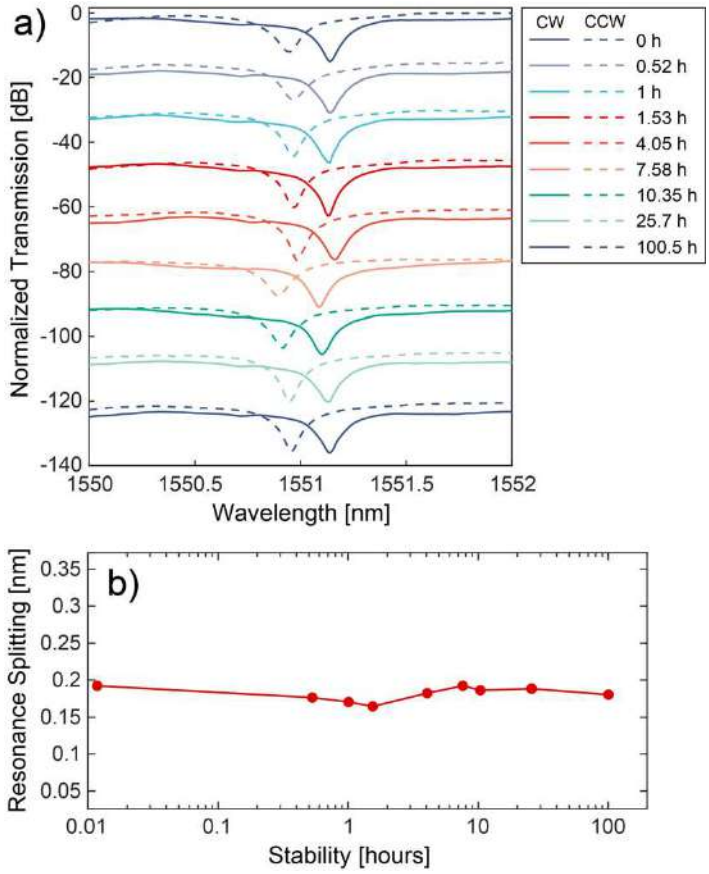

Figure S10: a) CW and CCW transmission spectra after programming for time intervals up to 4 days showing good nonvolatile stability of the devices after programming. **b)** Relative resonance shift between the CW and CCW modes in **a)**.

Additionally, we have completed extensive measurements to demonstrate the endurance of our devices for over 2.4 billion switching cycles. This endurance is more than 3 orders of magnitude improvement compared to other nonvolatile photonic memory platforms and is shown in Figure 5 of the main text. During this 3-day measurement, an arbitrary function generator was programmed to generate sequential +1V and −1V pulses which were then amplified to ±5V with an electronic amplifier (500 ns pulse width). Figure S11 shows time-domain measurements of both the optical transmission and electrical pulses used to cyclically write and erase data to the microring resonator with integrated CoFeB patterned magnetic stripes and electromagnet. Note the voltage and pulse width are limited by the slower, low-current pulse generator used rather than the device itself.

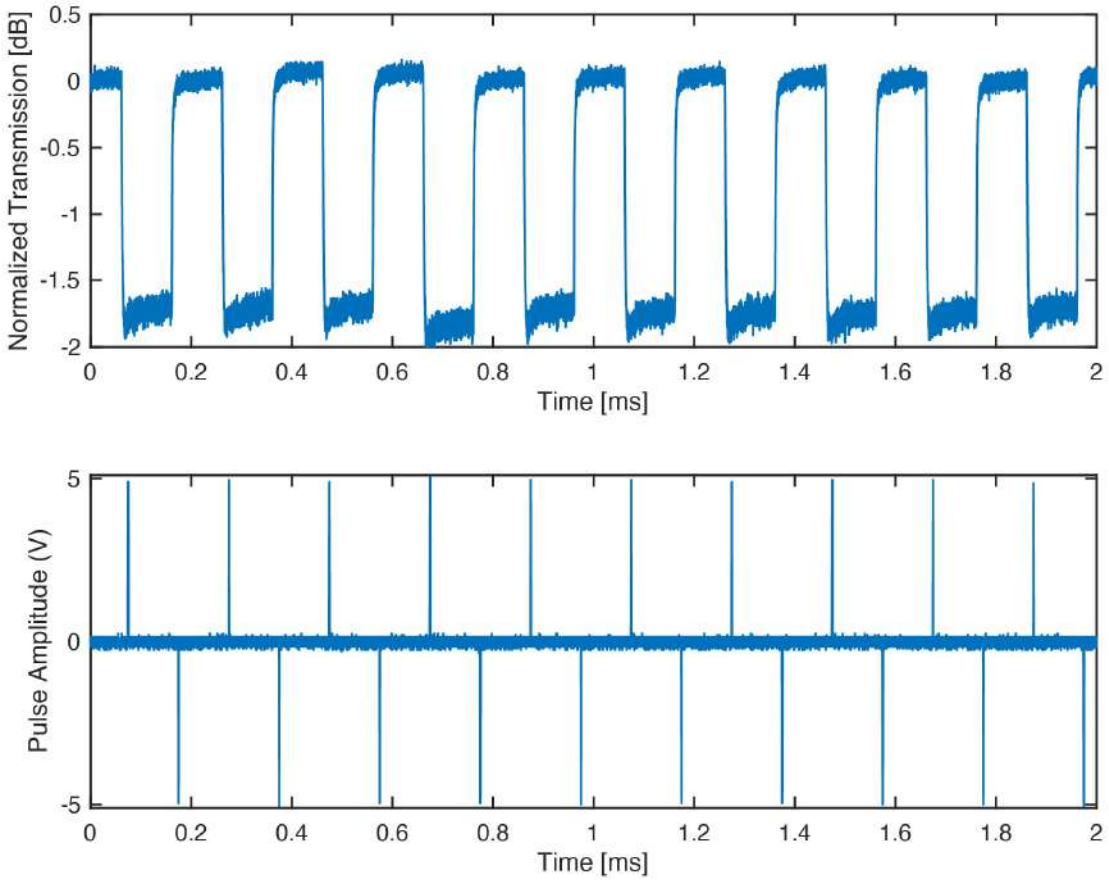

Figure S11: Time domain measurements of optical transmission (top) during nonvolatile switching with sequential write and erase pulses (bottom).

3. Thermo-optic and magneto-optic dynamic response

The thermo-optic and magneto-optic dynamic responses of the memory cell are characterized using the setup presented in section 2.1. To accurately estimate the rise and fall times of the responses, we fitted the experimental thermo-optic response with a first-order system, while the magneto-optic response is fitted using a second-order response with two complex conjugate roots.

3.1. Thermo-optic response

To evaluate the dynamic behavior of the thermo-optic response, we employed a square wave as an input stimulus with a period of $2 \cdot T_s$ where T_s=1 ms, and a duty-cycle of 50%. The corresponding output is modelled using the following expression:

$$y_{TO}(t) = C + A\,h(t-t_d) + B\left[1 - e^{-\frac{(t-t_d)}{\tau_\mathrm{r}}}\right]h(t-t_d) \\ -A\,h(t-t_d-T_s) - B\left[1 - e^{-\frac{(t-t_d-T_s)}{\tau_\mathrm{f}}}\right]h(t-t_d-T_s) \qquad (11)$$

where h(t) is the Heaviside step function, and t_d is the time delay of the thermal response. The terms multiplied by A are used to model the magneto-optic response, which is instantaneous with respect to the timescale of the thermal response. The terms multiplied by B reproduce the thermal response, where τ_r and τ_f are the rise and fall times, respectively. The last term C is included to account for any bias in the response.

The experimental results are fitted using a nonlinear least-squares curve-fitting algorithm implemented in MATLAB. We employ 5 terms as free parameters: A, B and C, and the rise and fall time constants, τ_r and τ_f. From the fitting, we estimated τ_f = 92 μs and τ_r = 50 μs.

3.2. Magneto-optic response

Similar to the previous case, we drive the device with a square wave having a period $2 \cdot T_\mathrm{f}$, where T_f=10 ns, and the duty-cycle is equal to 50%. For fitting the magneto-optic response, we employed a second-order response to account for both the initial oscillatory behavior and the damping [16]:

$$y_{MO}(t) = D + E\left[1 - e^{-\zeta\omega_n(t-t_d)}\right]cos\left(\omega_n\sqrt{1-\zeta^2}(t-t_d)\right)h(t-t_d) \\ -E\left[1 - e^{-\zeta\omega_n(t-t_d-T_\mathrm{f})}\right]cos\left(\omega_n\sqrt{1-\zeta^2}(t-t_d-T_\mathrm{f})\right)h(t-t_d-T_\mathrm{f}) \qquad (12)$$

In the equation, the terms multiplied by E reproduce the dynamic magneto-optic response, where ω_n is the natural angular frequency, ζ is the dimensionless damping factor [16]. The terms ω_n and ζ are related to the response of the magneto-optic material. The rise/fall time is given by $(\zeta\omega_n)^{-1}$ while the frequency observed in the system is the damped natural frequency $\omega_n\sqrt{1-\zeta^2}$, which is the precession of the magnetic moment in the material called Larmor precession frequency or ferromagnetic resonance. Differently from the thermo-optic response, we have not assumed any

differences between the rise and fall time. As before, the term D is included to account for any bias in the response.

The value of ω_n = 3.6 Grad/s and ζ = 0.29 are obtained fitting the experimental curve using 4 free parameters (i.e., D, E, ω_n and ζ). Using this result, we estimate a rise/fall time equal to 0.95 ns, while the Larmor precession frequency (i.e., the damped natural frequency of the second order system) is equal to 0.55 GHz.

The results of the fitting lead us to conclude that the magneto-optic response of the device is limited by the Ce:YIG and not by the driving circuit. Indeed, the rise/fall time estimated from the fitting is larger than the time response of the RL circuit, which can be estimated from the electrical characterization of the electromagnet. Specifically, by measuring the electrical back-reflection (S_{11} coefficient) of the Au coil, we obtain R = 1.43 Ω and L = 0.3 nH. Considering the impedance of the driver is Z = 50 Ω, the response time of the RL circuit is $\tau_C = L/(R + Z)$ = 5.8 ps.

Although the time response of this device is limited to 1GHz, a much faster response can be accomplished with other magneto-optic materials. For instance, cadmium manganese telluride ($Cd_{1-x}Mn_xTe$) can support a modulation rate of tens of gigahertz [17], [18].

4. Memory bit resolution of magneto-optic memory cell

One of the advantages of the proposed integrated optical memory is its large data capacity that can be stored. In this section, we quantify the maximum number of bits that can be memorized in the proposed device. For this analysis, we consider a magneto-optic memory cell based on the all-pass microring shown in Figure 1b of the manuscript and shown in Figure S12 for the sake of clarity.

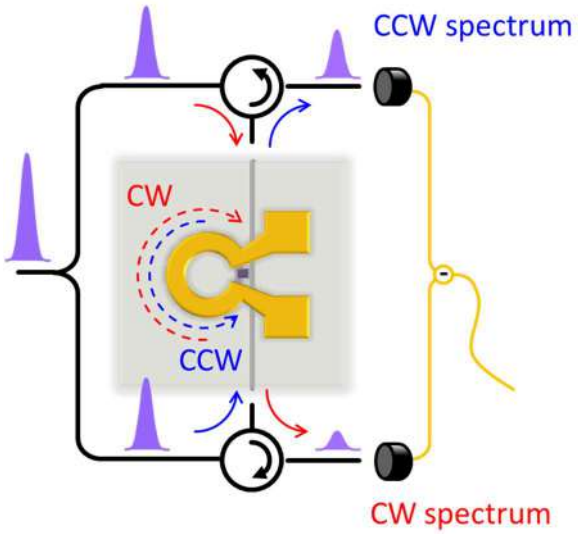

Figure S12. Magneto-optic memory cell based on all-pass ring resonator configuration.

A different resonance tuning of the microring implies a different status of the memory. The precision of the tuning is influenced by the phase variation of the microring, which includes thermo-refractive noise (TRN) and magnetic field fluctuations (MFF). On the other hand, accurate power readings at the CW and CCW photodiode can be a challenge when we need to detect a small change of the memory status (i.e., a small resonance variation). A correct reading of the memory is limited by the thermal noise and shot noise of the photodetectors as well as the relative intensity noise of the laser (RIN). Considering all this contribution, the value of the power measured at the photodetectors (PDs) is subject to a total variation that can be written as

$$\Delta P^{\pm} = \Delta P_{\mathrm{TRN}} + \Delta P_{\mathrm{MFF}} + \Delta P_{\mathrm{PD\,therm}} + \Delta P_{\mathrm{shot}} + \Delta P_{\mathrm{RIN}} \tag{13}$$

where the signs $\pm$ refer to the PD that is used to detect the CW and CCW mode, respectively.

4.1. Power variation with respect to phase noise

The phase variation in the microring leads to a fluctuation in the power measured at the PDs. To establish the relationship between the phase variation and the output power, we begin with the transfer function in Eq. (9). The power measured at the PDs depends on the power injected from the laser, P_{in}, the round-trip loss, $1 - a^{\pm}$, and the round-trip phase in the cavity, $\phi^{\pm}$, where $\pm$ indicate the CW and CCW mode, respectively

$$P^{\pm} = |T^{\pm}|^2 P_{in} = \frac{(a^{\pm})^2 - 2ra^{\pm}\cos\phi^{\pm} + r^2}{1 - 2ra^{\pm}\cos\phi^{\pm} + (ra^{\pm})^2} P_{in} \tag{14}$$

Considering the TRN and the MFF as an additive term on the phase, $\Delta\phi$, the previous equation becomes

$$P^{\pm} + \Delta P^{\pm} = \frac{(a^{\pm})^2 - 2ra^{\pm}\cos(\phi^{\pm} + \Delta\phi) + r^2}{1 - 2ra^{\pm}\cos(\phi^{\pm} + \Delta\phi) + (ra^{\pm})^2} P_{in} \tag{15}$$

For the MFF we neglect the loss variation induced by the magnetic field fluctuation since this contribution is smaller than then one inducted on the phase. Assuming that $\Delta\phi$ is a small perturbation, we can explicit the power variation induced by the phase fluctuation in the cavity as

$$\Delta P^{\pm} = \frac{2ra^{\pm}(1 - r^2)[1 - (a^{\pm})^2]\, sin\,\phi^{\pm}}{\{[1 + (ra^{\pm})^2] - 2ra^{\pm}\, cos\,\phi^{\pm}\}^2} \cdot P_{in} \cdot \Delta\phi \tag{16}$$

Since the device operates near resonance and we can control the phase with the magneto-optic effect, we can express the phase as $\phi^{\pm} = 2\pi n \pm \Delta\phi_{MO}$, where $\Delta\phi_{MO} > 0$ is the amplitude of the non-reciprocal phase shift. Consequently, the previous expression simplifies as follows:

$$\Delta P^{\pm} \simeq \pm \frac{2ra^{\pm}(1 - r^2)[1 - (a^{\pm})^2]\,\Delta\phi_{MO}}{[(1 - ra^{\pm})^2 + ra^{\pm} \cdot \Delta\phi_{MO}^2]^2} \cdot P_{in} \cdot \Delta\phi \tag{17}$$

This formula is central to our analysis, as it will be used to compute the maximum number of bits that can be memorized in a single memory cell. Although in Eq. (17) we indicate the phase variation induced by the noise, we can easily convert the fluctuation in terms of wavelength, recalling that a phase shift of 2π is equivalent to a wavelength variation of a free-spectral range (FSR):

$$\Delta\phi = \frac{2\pi}{FSR} \cdot \Delta\lambda \tag{18}$$

4.2. Thermal noise of the photodetector

Thermal noise can also directly impact the PDs due to thermal fluctuations occurring within electron density. Its common expression is

$$\Delta P_{\mathrm{PD\ therm}} = 4k_B TB \tag{19}$$

where T is the temperature, k_B is the Boltzmann constant, and B is bandwidth of the PD.

4.3. Shot noise

Shot noise arises in situations involving potential barriers, such as within a pn-junction of a PD, and stems from the discrete nature of electron charge. The common expression for this noise is

$$\Delta P_{\text{shot}} = R \cdot 2qIB \tag{20}$$

where q is the elementary charge of an electron, while R and I are the resistance and the average current flowing the PD, respectively.

4.4. Relative intensity noise

Computing the power fluctuation at the PD generated by the laser relative intensity noise is straightforward using the expression in Eq. (15). Assuming $P_{in} = P_0 + \Delta P_{in}$ and $\Delta\phi = 0$, the expression can be simplified using $\phi^{\pm} = 2\pi n \pm \Delta\phi_{MO}$ such that:

$$\Delta P_{\text{RIN}} = \frac{(a^{\pm} - r)^2 + ra^{\pm} \cdot \Delta\phi_{MO}^2}{[(1 - ra^{\pm})^2 + ra^{\pm} \cdot \Delta\phi_{MO}^2]} \cdot P_0 \cdot \text{RIN} \tag{21}$$

where $\text{RIN} = \Delta P_{in}/P_0$ and ΔP_{in} is the fluctuation of the laser power. The RIN affects both photodetectors (PDs) in the same manner since it depends on the square of the non-reciprocal phase shift. Utilizing the configuration shown in Figure S12, the common mode of the noise in the two PDs cancels out, rendering the contribution of RIN negligible in this configuration.

4.5. Numerical results

Using the model presented in the previous section, we have numerically evaluated all the noise contributions. First, we simulated the root mean square of the power spectral density of the phase variation due to the thermo-refractive noise and thermal-magnetic fluctuation. The results are show in Figure S13.

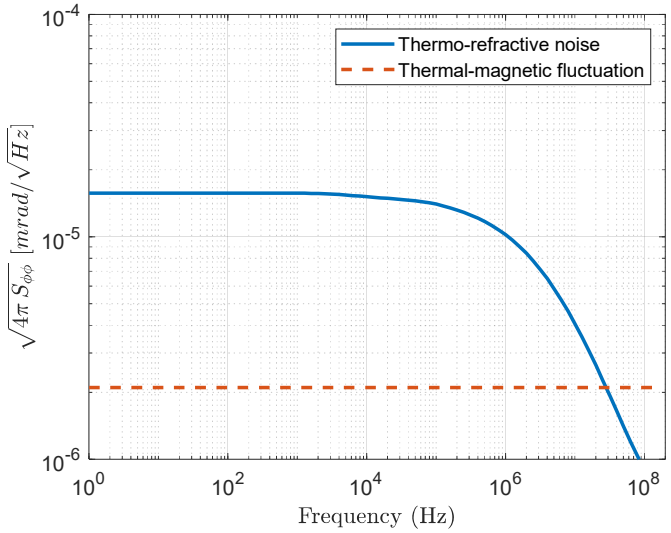

Figure S13. Phase noise spectral density of the thermo-refractive noise and thermal-magnetic fluctuation.

The thermo-refractive noise is the dominant contribution to the phase and is primarily produced by the large thermo-optic coefficient of the silicon waveguide. The phase variation induced by the thermal-magnetic fluctuation in the Ce:YIG is one order of magnitude smaller than the thermo-refractive noise (TRN), and it can be neglected.

Using Eq. (17), we can convert the phase noise spectral density shown in Figure S13 into the corresponding power spectral density measured at a single photodetector. The two source of phase noise together with noise of the PD and the RIN of the laser are shown in Figure S14. As it appears clear, the thermo-refractive noise is the dominant contribution.

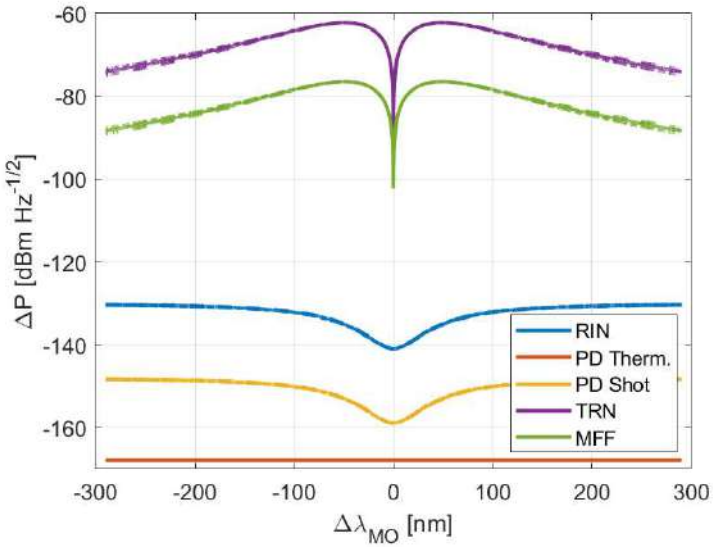

Figure S14. Power spectral density at a single photodetector as a function of the resonance offset induced by the non-reciprocal phase shift effect. All the contributions have been considered at room temperature. We assumed the PD resistance is equal to 1 kΩ and the responsivity is 0.5 A/W. The input power of the

laser is P_{in} = 13dBm while the RIN is -140 dBc/Hz. For each noise contribution, we plot the CW (dot-dashed line), the CCW (dashed line) and the case where the nonreciprocal loss is neglected (continuous line). There is no significant difference of the three cases.

Using Eq. (17), we have converted the shot noise, the thermal noise, and the RIN into the equivalent phase noise at the resonators. The results are shown in Figure S15.

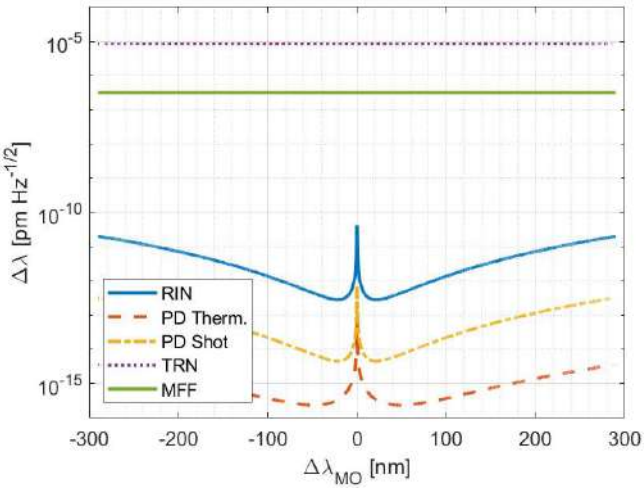

Figure S15. Phase noise spectral density as a function as a function of the resonance offset induced by the non-reciprocal phase shift effect.

Considering thermo-refractive noise —the dominant noise contribution— we can now estimate the maximum number of bits that can be stored in the proposed magneto-optic memory cell.

From the phase noise spectral density of the thermo-refractive noise shown in Figure S13 we can estimate the variance of the resonance $\Delta\phi$=2.85·10^{-5} rad, which corresponds to a wavelength variation of $\Delta\lambda$ = 0.0155 pm. On the other hand, the maximum wavelength shift due to the MO effect is ±290pm.

Assuming the levels are spaced by 3 times sigma, the number of bits is 13.6 bits:

$$\#\text{bits} = \log_2\left(\frac{Range}{3\Delta\lambda}\right) = 13.6 \qquad (22)$$

5. References

[1] M. Chrostowski, Lukas; Hochberg, *Silicon Photonics Design*. Cambridge University Press, 2015.

[2] P. Pintus, 'Accurate vectorial finite element mode solver for magneto-optic and anisotropic waveguides', *Optics Express*, vol. 22, no. 13. p. 15737, 2014. doi: 10.1364/OE.22.015737.

[3] P. Pintus *et al.*, 'PWM-Driven Thermally Tunable Silicon Microring Resonators: Design, Fabrication, and Characterization', *Laser Photon Rev*, vol. 13, no. 9, Sep. 2019, doi: 10.1002/lpor.201800275.

[4] H. Dötsch *et al.*, 'Applications of magneto-optical waveguides in integrated optics: review', *Journal of the Optical Society of America B*, vol. 22, no. 1, p. 240, Jan. 2005, doi: 10.1364/JOSAB.22.000240.

[5] W. Zaets and K. Ando, 'Optical waveguide isolator based on nonreciprocal loss/gain of amplifier covered by ferromagnetic layer', *IEEE Photonics Technology Letters*, vol. 11, no. 8, pp. 1012–1014, Aug. 1999, doi: 10.1109/68.775330.

[6] D. Huang *et al.*, 'Dynamically reconfigurable integrated optical circulators', *Optica*, vol. 4, no. 12, p. 23, 2017, doi: 10.1364/optica.4.000023.

[7] COMSOL multiphysics, 'www.comsol.com'. [Online]. Available: https://www.comsol.com/

[8] H. Dötsch *et al.*, 'Applications of magneto-optical waveguides in integrated optics: review', *Journal of the Optical Society of America B*, vol. 22, no. 1, p. 240, 2005, doi: 10.1364/JOSAB.22.000240.

[9] M. C. Onbasli *et al.*, 'Optical and magneto-optical behavior of Cerium Yttrium Iron Garnet thin films at wavelengths of 200–1770 nm', *Sci Rep*, vol. 6, no. 1, p. 23640, Mar. 2016, doi: 10.1038/srep23640.

[10] P. Pintus, D. Huang, C. Zhang, Y. Shoji, T. Mizumoto, and J. E. Bowers, 'Microring-based optical isolator and circulator with integrated electromagnet for silicon photonics', *Journal of Lightwave Technology*, vol. 35, no. 8, pp. 1429–1437, 2017, doi: 10.1109/JLT.2016.2644626.

[11] P. Pintus *et al.*, 'An integrated magneto-optic modulator for cryogenic applications', *Nat Electron*, vol. 5, no. 9, pp. 604–610, 2022, doi: 10.1038/s41928-022-00823-w.

[12] W. Bogaerts *et al.*, 'Silicon microring resonators', *Laser Photon Rev*, vol. 6, no. 1, pp. 47–73, 2012.

[13] J. Heebner, R. Grover, T. Ibrahim, and T. A. Ibrahim, *Optical microresonators: theory, fabrication, and applications*. Springer Science & Business Media, 2008.

[14] J. Capmany, P. Munoz, J. D. Domenech, and M. A. Muriel, 'Apodized coupled resonator waveguides', 2007. doi: 10.1364/OE.15.010196.

[15] J. Igarashi *et al.*, 'Single-nanometer CoFeB/MgO magnetic tunnel junctions with high-retention and high-speed capabilities', *npj Spintronics*, vol. 2, no. 1, p. 1, Jan. 2024, doi: 10.1038/s44306-023-00003-2.

[16] K. Ogata, *System Dynamics*, IV Ed. 2004.

[17] M. R. Freeman, 'Picosecond pulsed-field probes of magnetic systems (invited)', *J Appl Phys*, vol. 75, no. 10, pp. 6194–6198, 1994, doi: 10.1063/1.355454.

[18] R. Rey-De-Castro *et al.*, 'Subpicosecond Faraday effect in Cd 1-xMn xTe and its application in magneto-optical sampling', *Appl Phys Lett*, vol. 85, no. 17, pp. 3806–3808, 2004, doi: 10.1063/1.1809280.